Numerical modelling of brittle fracture using lattice particle method with applications to fluid structure interaction problems via SPH coupling

K.C. Ng [a,*], Hailong Chen [b]

[a] *Department of Mechanical, Materials and Manufacturing Engineering, University of Nottingham Malaysia, Jalan Broga, 43500 Semenyih, Selangor Darul Ehsan, Malaysia*
[b] *Department of Mechanical and Aerospace Engineering, University of Kentucky, Lexington, KY 40506, USA*

ARTICLE INFO

ABSTRACT

This paper presents an improved failure model for simulating brittle fracture using the mesh-less Lattice Particle Method (LPM). By modelling the initial crack line using the Remove Bond (RB) approach as outlined in this paper, a new formulation is then developed for predicting the mode-I Stress Intensity Factor (SIF) near the crack tip. Compared to the conventional Remove Particle (RP) approach, it is found that the accuracy of the present SIF formulation based on the RB method is superior. A series of benchmark test cases are simulated to test the numerical accuracy and numerical convergence of the method. Finally, the LPM method is coupled with the Smoothed Particle Hydrodynamics (SPH) method for studying Fluid Structure Interaction (FSI) problems involving solid fracture and free surface. The coupled SPH-LPM method is implemented in the open-source code, DualSPHysics, which has been optimized for both CPU and GPU performances. Upon integrating LPM with SPH, the proposed FSI method is suitable for modelling fracture phenomena caused by natural hazards such as tsunami and flood.

1. Introduction

Fluid-structure interaction (FSI) problems are widely encountered in various engineering applications. Failing to consider the FSI effect could be disastrous and lead to unexpected structural failure. One of the famous examples is the collapse of the Tacoma Narrows Bridge due to aeroelastic flutter. Nowadays, due to the advancement of computing architecture, many advanced numerical schemes have been developed within the Computational Fluid Dynamics (CFD) and Computational Solid Mechanics (CSM) communities for analyzing challenging FSI problems. In general, there are two main computational approaches used to model FSI problem, i.e., monolithic, and partitioned approaches. Monolithic approach solves the fluid and solid governing equations simultaneously using a single solver. For partitioned approach, however, a specific solver for each fluid and solid domain are coupled; hence, the software modularity of each existing solver that has been well tested for either fluid equation or solid equation could be preserved. The current work employs the partitioned approach in FSI modelling.

Numerical schemes developed for solving FSI problems are typically mesh-based in nature where the problem domain is discretized with a series of interconnected polygons. Most of these mesh-based schemes are developed based on the numerical frameworks of

---

* Corresponding author.
E-mail addresses: khaiching.ng@nottingham.edu.my, ngkhaiching2000@yahoo.com (K.C. Ng).

Finite Element Method (FEM) [1,2] and Finite Volume Method (FVM) [3]. To model FSI problems involving large structural deformation using body conformal grid, an additional remeshing [4] procedure is often required so that the local mesh quality is not seriously deteriorated at the expense of higher computational cost. The overset grid method could be used to address FSI problem without remeshing [5]; however, its accuracy is dependent on the interpolation error level at the grid interface which could be high if large gradient is involved. The original immersed-boundary (IB) method of Peskin [6], which is one of the non-body conformal methods, involves a background Cartesian grid laid behind a solid body. The force interaction between the fluid and solid bodies is realized using a smoothed forcing term from the immersed solid boundary nodes, in which the interpolation accuracy is dependent on the mesh size. Other more accurate IB method that utilizes cut-cell method [7] near the solid boundary could be employed; however, special numerical treatments are needed at meshes close to the solid boundary and discretization of flow equations at those meshes is often non-trivial. The use of mesh-based method in FSI modelling is further complicated if free surface is involved. For example, the conventional level-set method suffers from mass conservation issue during the time evolution of the level-set function and special numerical treatment is often required to address this issue [8]. Also, it is numerically challenging for the Volume of Fluid (VOF) method to capture (or geometrically construct) the location of highly fragmented free surface on a fixed Eulerian mesh. In short, mesh-based method may require extensive remeshing and/or data interpolation procedures while modelling FSI problem involving large structural deformation and free surface.

To address the limitations of mesh-based methods mentioned above, many mesh-less/particle methods have been developed and applied to model FSI problems involving large structural deformation and violent free surface flow. One of the widely used particle methods is Smoothed Particle Hydrodynamics (SPH) that was originally used for modelling astrophysical problem [9,10] and later extended by Monaghan [11] to simulate free surface flow. For modelling FSI problem involving large structural deformation, both fluid and solid bodies could be modelled using SPH [12–14], or the SPH fluid solver could be coupled with other structural solvers such as FEM [15–17] and Total-Lagrangian SPH (TLSPH) [18–21]. These structural solvers are generally developed based on continuum mechanics theory and might face difficulties while simulating solid fracture and fragmentation which involves spatial discontinuities, as these schemes are prone to numerical errors and crack-tip singularities due to the presence of spatial derivatives [22].

As a remedy to the limitation of continuum mechanics theory-based methods in fracture modelling, some discontinuous structural solvers such as Discrete Element Method (DEM) [23–25] and Peridynamics (PD) [22,26] that do not depend on partial differential equations have been recently coupled with SPH for simulating FSI problems involving solid fracture. Some two-dimensional test cases have been simulated using the SPH-DEM schemes [23,24] as well as the recently proposed SPH-PD schemes of Yao and Huang [26] and Rahimi and co-workers [22], although these schemes presented can be readily extended to 3D. In fact, as compared to most of the existing SPH-PD schemes, the very recent SPH-PD scheme of Yao and Huang [26] features a more accurate FSI coupling scheme that satisfies momentum conservation. In their work [26], PD particles are treated as either repulsive or ghost/dummy particles in the support domain of a SPH particle near the fluid–structure interface. Momentum conservation is then satisfied by enforcing force balance between the SPH and PD particles near the interface. In fact, the coupling scheme that satisfies momentum conservation has been previously implemented in our SPH-Lattice Particle Method (SPH-LPM) scheme [27] for simulating FSI problems. Although LPM can be regarded as a lattice-spring model like DEM, it was originally proposed by Chen and co-workers [28] to address the difficulties of DEM in simulating problems with a wider range of Poisson ratio. For solid mechanics problem, LPM has demonstrated its uniqueness and robustness in simulating fracture problems [28,29]. However, while modelling brittle fracture using LPM, tuning is often performed to determine the suitable critical stretch (or strain) via numerical tensile test.

It is generally known that for ensuring numerical convergence while modelling brittle fracture problem, the fracture mechanics-based approach should be considered [30]. By modelling the initial crack line via removing a single layer of SPH particles (denoted as Remove Particle (RP) approach in this paper), Ganesh and co-workers [31] have recently shown that the mode-I Stress Intensity Factor (SIF) near the crack tip converges to the theoretical value (for a specific loading and initial crack configuration) as the particle resolution is refined. However, there is a lack of theoretical detail on how their SIF formula is derived. Separately, Tazoe and co-workers [32,33] have formulated a simple mode-I SIF (K_I) formula based on the maximum principal stress and the diameter of the crack front particle. Although the crack propagation pattern is well captured, their computed K_I value is apparently higher than the theoretical result. This could be attributed to the difficulty in getting an accurate stress value near the crack tip due to stress singularity.

In the current work, inspired from the work of Tazoe and co-workers [32,33], a different way of modelling the initial crack line is pursued. Instead of removing a layer of particles to model the initial crack line (i.e., RP approach), the bonds of the respective particles representing the initial crack line are removed instead. We denote this approach as Remove Bond (RB) approach in this paper. To support this modelling approach, a new mode-I Stress Intensity Factor (SIF) formulation is developed, as the crack front particles are now oriented at 45° from the crack line. The above formulation is implemented in our previous LPM solver, upon which the numerical accuracy and numerical convergence are tested by using a series of static and dynamic fracture mechanics benchmark test cases. We then incorporate the above failure model in our SPH-LPM method [34] to simulate 2D FSI problems involving solid fracture. Mode-I brittle fracture, i.e., without considering plastic deformation, is the focus of the present study. For certain problems, when fresh non-bonded particles appear on newly formed crack surfaces, the possible collision between these particles are handled using a penalty approach. The current method is implemented in the open-source WCSPH code, DualSPHysics, which has been optimized for both CPU and GPU performances. As the fluid pressure is solved explicitly in the numerical framework of WCSPH, the WCSPH method is very attractive for large scale computation.

The remainder of this paper is organized as follows. Firstly, in Section 2, the LPM method for solid modelling is presented, followed by a detailed discussion of brittle fracture model based on Stress Intensity Factor (SIF). The fluid modelling technique using SPH is then shown, followed by its coupling with the LPM method for FSI modelling. In Section 3, the proposed SIF formula is verified, and the present LPM solid fracture model is tested by comparing the simulated crack patterns against the published experimental and
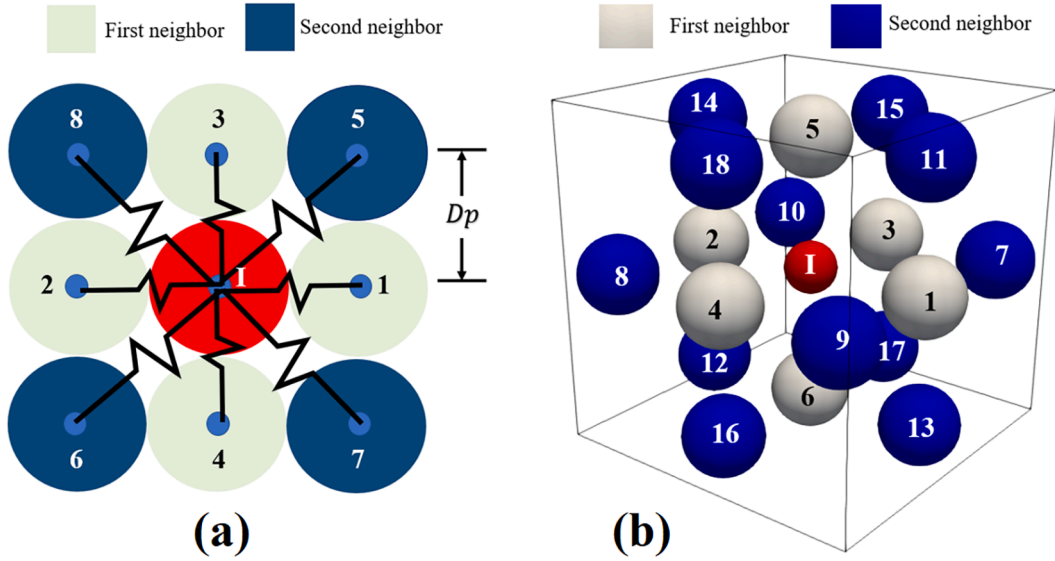
Fig. 1. (a) 2D square (a) and (b) 3D simple cubic lattice structure used in LPM for domain discretization [36]. D_p is particle size.

numerical data obtained from the literature. Following this, several FSI problems involving brittle fracture are modelled to validate the proposed model. Some concluding remarks are made in Section 4, together with some recommendations for future work. This paper ends with a brief discussion of our on-going attempt to simulate fracture of a real 3D concrete structure due to tsunami, in which some preliminary numerical results on the validation against the experimental data are presented in the Appendix.

2. Mathematical models and numerical methods

2.1. Solid model

The Lattice Particle Method (LPM) (or known as Volume Compensated Particle Method (VCPM)) has been implemented in DualSPHysics in our previous work [34] to model the deformation of linear elastic solid in FSI problems. LPM reformulates the classical continuum mechanics model using integro (spatial)-differential (temporal) equations by introducing 1D bond-level force–elongation relationship between discrete particles to avoid issues resulted from the continuity requirement from the partial differential equations. As depicted in Fig. 1 for the 2D square and 3D simple cubic lattice configuration, a solid particle I interacts with its first and second neighbours via 1D bonds. The equation of motion of a solid particle I can be written as:

$$m_I \frac{d\mathbf{v}_I}{dt} = \mathbf{F}_{S,I} + \mathbf{F}_{F \to S,I} + \mathbf{F}_{ext,I}, \tag{1}$$

where m_I is mass of solid particle I, $\mathbf{v}_I$ is the velocity of solid particle I, $\mathbf{F}_{S,I}$ is the net bonding force (due to neighbouring solid particles), $\mathbf{F}_{F \to S,I}$ is the hydrodynamic force acting on a solid particle I (to be discussed later) and $\mathbf{F}_{ext,I}$ is any external force vector (e.g., gravity, solid–solid collision force, etc.).

The net bonding force acting on a solid particle I, $\mathbf{F}_{S,I}$ can be determined as:

$$\mathbf{F}_{S,I} = \sum_J f_{IJ} \hat{\mathbf{u}}_{IJ}, \tag{2}$$

where $\hat{\mathbf{u}}_{IJ} = (\mathbf{r}_I - \mathbf{r}_J)/\|\mathbf{r}_I - \mathbf{r}_J\|$ is the unit bond vector and f_{IJ} is the bond force that has the following explicit form:

$$f_{IJ} = -(1 - D_{IJ})k\delta L_{IJ} - T\left(\sum_Q (1 - D_{IQ})\delta L_{IQ} + \sum_M (1 - D_{JM})\delta L_{JM}\right). \tag{3}$$

Here, δL_{IJ} is the bond elongation between solid particles I and J. The subscripts Q and M indicate the neighbours of particles I and J, respectively. The bond stiffness k can be determined by ensuring energy equivalency between the LPM description and its continuum counterpart [35] based on Young's modulus E and solid Poisson ratio v^s. A non-local parameter T is introduced as well to remove the restriction of Poisson ratio [35]. The complete k and T formulations for 2D and 3D linear elastic solid bodies can be found from our previous works [27,28,35]. To monitor the state of the bond between two particles in modelling solid fracture problems, a bond damage parameter D_{IJ} between solid particles I and J is introduced, which is further explained in the following section.
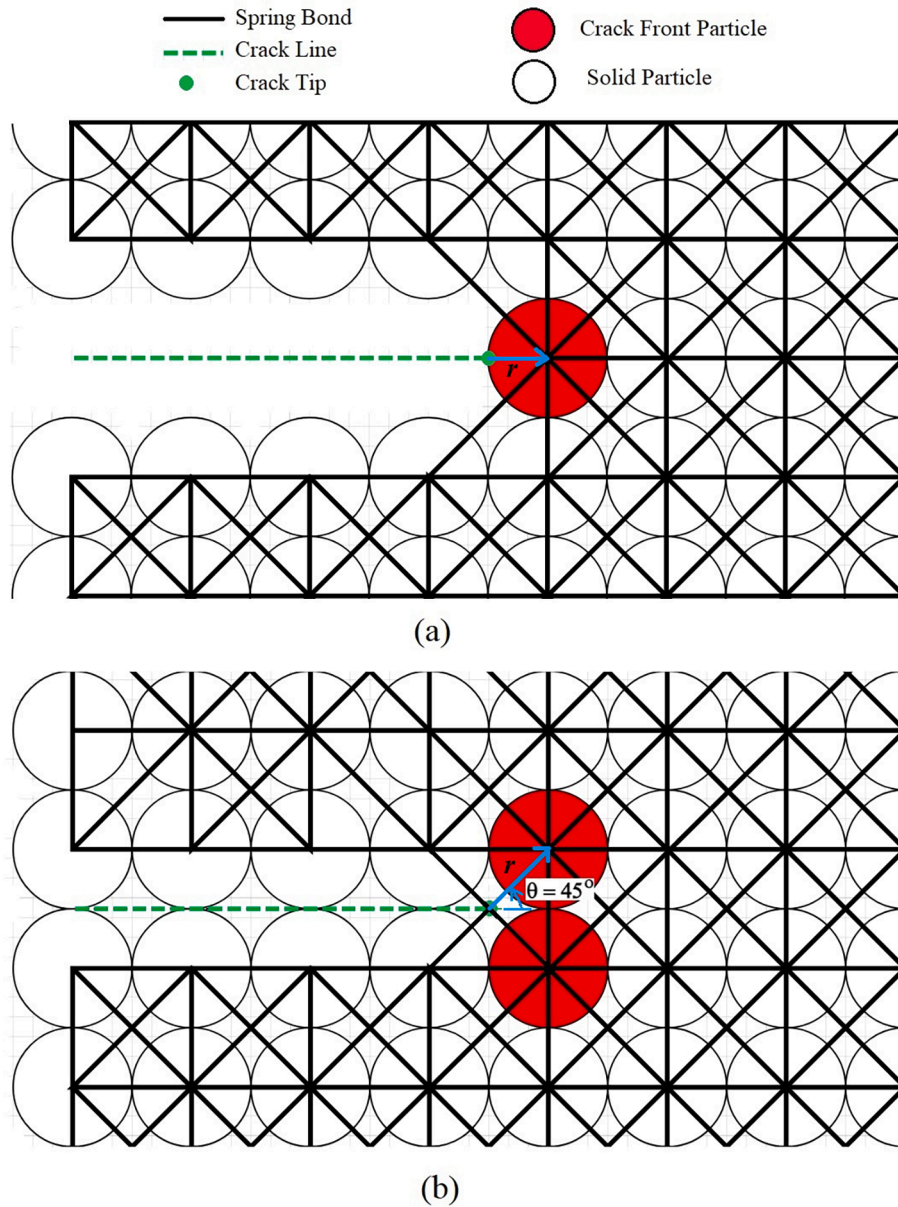
Fig. 2. Methods of modelling the initial crack line. (a) Remove Particle (RP) and (b) Remove Bond (RB). Note that the locations of crack front particles are meant for Mode-I loading.

2.1.1. Solid fracture model

To simulate brittle fracture, there are several criteria available to determine the bond damage parameter. For example, the critical force criterion [29,37,38] states that a bond is broken ($D_{IJ} = 1$) if the force developed within a spring bond exceeds the critical force within the bond. Here, the critical force is determined from the critical stress value obtained from the respective uniaxial tensile test. Other criterion such as critical elongation [35] has been proposed as well, where the bond is broken if the bond elongation exceeds a critical elongation value. The critical elongation value, however, is case-dependent and calibration is needed. In other meshfree method such as Peridynamics (PD), the critical elongation is related to the critical energy release rate and is horizon size dependent.

The stress-based approach such as Rankine criterion has been recently adopted in particle method such as SPH [39] to model brittle fracture. When the maximum principal stress of a particle exceeds the material ultimate tensile strength, the particle becomes completely damaged and no longer interacts with other particles. Separately, Wiragunarsa and co-workers [40] have found that the crack growth direction can be predicted accurately by tracking the neighbouring particle with the highest maximum principal stress. Despite the simplicity of Rankine criterion, its implementation alone in simulating the brittle fracture of a pre-notched specimen would lead to the under-prediction of failure load at refined particle resolution [30]. This is attributed to the fact that the maximum principal

stress becomes infinitely large (in the context of Linear Elastic Fracture Mechanics (LEFM), where plasticity is assumed to be absent near the crack tip) as the particle size decreases. In other words, numerical convergence could not be assured if only the Rankine criterion alone is considered for brittle fracture modelling.

To ensure numerical convergence of brittle fracture modelling, Tavarez and Plesha [30] have incorporated both the Rankine and fracture mechanics criteria in their DEM modelling. Specifically, two parameters are required in their fracture model, i.e., ultimate tensile strength, σ_{UTS} and fracture toughness, $K_{I,C}$. Very recently, by using SPH, Ganesh and co-workers [31] have demonstrated the numerical convergence of mode-I Stress Intensity Factor (SIF), K_I at the crack front particle near an initial crack line. In general, there are two ways of modelling an initial crack line as shown in Fig. 2, i.e. (a) Remove Particle (RP); and (b) Remove Bond (RB) methods, where recent works such as [31,32] have witnessed the use of RP method in modelling an initial crack line. Based on the Westergaard's Mode-I crack formulation, near the crack tip, the normal stress σ_n (perpendicular to the crack line) of a crack front particle can be approximated as:

$$\sigma_n = \frac{K_I}{\sqrt{2\pi r}} C,$$
(4)

where $C = cos\frac{\theta}{2}\left(1 + sin\frac{\theta}{2} sin\frac{3\theta}{2}\right)$. Here, r and θ are the radial distance and angular position of the crack front particle from the crack tip (see Fig. 2), respectively. For the RP model considered by Tazoe and co-workers [32] (Fig. 2(a)), $r = D_p/2$ and $\theta = 0^o$ and hence $C = 1$. Here, D_p is the particle size. Recently, both [31,32] further reported that σ_n could be modelled as the maximum principal stress σ_1 for Mode-I fracture and good accuracy in K_I estimation has been reported in the recent work of [31]. Hence, the mode-I SIF, K_I, can be further simplified as [32]:

$$K_I = \sigma_1\sqrt{\pi.D_p}.$$
(5)

In the current work, Eq. (5) is implemented in LPM and the results are tested against those of [32]. In addition, the RB modelling of initial crack line (Fig. 2(b)), which is not considered in recent attempts [31,32], is implemented in the current work as well. By setting $r = D_p/\sqrt{2}$ and $\theta = 45^o$ in Eq. (4), the mode-I SIF, K_I for the RB model can be computed as:

$$K_I = \frac{8\sqrt[4]{2}}{\left(4+\sqrt{2}\right)\sqrt{\left(2+\sqrt{2}\right)}}\sigma_1\sqrt{\pi.D_p} \sim 0.951\sigma_1\sqrt{\pi.D_p}.$$
(6)

It is important to note that Eq. (6) is only applicable for pure Mode-I loading, i.e., the applied external force direction is orthogonal to the crack line. For cases where the external load is not acting perpendicular to the crack line, the crack front particle (for RB case) may be no longer located at $r = D_p/\sqrt{2}$ and $\theta = 45^o$ from the crack tip. As such, the R.H.S. of Eq. (4) should be expanded [41] accordingly to consider the SIFs of other modes of fracture and this is left for future development.

When cracks are present in a specimen, the stress near the crack tip would reach the material's ultimate tensile strength rapidly (more rapid if particle resolution is refined) during loading condition. Nevertheless, failure should not happen if the Stress Intensity Factor (SIF) is below the material's fracture toughness. In the current work, inspired from [42], the maximum principal stress (Rankine) is merely used to determine the onset of fracture. A crack front particle is completely fractured only if:

$$K_I > K_{I,C}.$$
(7)

Similar to [39,40], a fractured particle will lose its interactions with its neighbouring particles by breaking the associated spring bonds. At the beginning of simulation, a spring bond between solid particles I and J is assumed as undamaged, i.e., the bond damage parameter is taken as $D_{IJ} = 0$. In this case, by evaluating Eq. (3), the interaction between particles I and J can be determined. When a fractured solid particle loses its interaction with its neighbours, the bond damage parameter D_{IJ} is changed to 1, which indicates crack is nucleated between the particles I and J and the bond is damaged. The interaction between two particles with damaged bond ceases completely and irreversibly. The crack path can then be traced explicitly through the damage state of each particle, e.g., particle I, as:

$$D_I = \frac{\sum_J D_{IJ}}{N_b},$$
(8)

where N_b is the total number of bonds connected to solid particle I at the beginning of simulation.

2.2. Flow model

The motion of an isothermal, incompressible fluid can be generally described using mass and momentum conservation equations:

$$\frac{d\rho}{dt} = -\rho\nabla.\mathbf{v}$$
(9)

and

$$\frac{d\mathbf{v}}{dt} = \frac{1}{\rho}\nabla P + \mathbf{E}$$
(10)

respectively. Here, ρ is the fluid density, $\mathbf{v}$ is the fluid velocity vector and $\mathbf{E}$ is the external acceleration vector (e.g., dissipation, gravity, etc.). In WCSPH, the equations governing mass and momentum conservation for each fluid particle i can be discretized as [43]:

$$\frac{d\rho_i}{dt} = \rho_i \sum_j V_j (\mathbf{v}_i - \mathbf{v}_j) \cdot \nabla_i W_{ij} + 2\delta h c^F D_i \tag{11}$$

and

$$m_i \frac{d\mathbf{v}_i}{dt} = \mathbf{F}_i, \tag{12}$$

respectively. Here, V is the fluid volume, m is the fluid mass, and $\mathbf{F}$ is the force vector. The gradient vector $\nabla_i W_{ij}$ is defined as $\nabla_i W_{ij} = \frac{dW_{ij}}{dr} \frac{\mathbf{r}_{ij}}{\|\mathbf{r}_{ij}\|}$ where $\mathbf{r}_{ij} = \mathbf{r}_i - \mathbf{r}_j$ is the position vector between particles i and j. In the current study, the Wendland [44] kernel function W_{ij} with a compact support radius $r_c = 2h$ is employed, where $h = 1.5 \times D_p$ is the smoothing length. The term $2\delta h c^F D_i$ is introduced in the R.H.S. of Eq. (11) to suppress the pressure noise in the WCSPH scheme where δ is the coefficient usually taken as 0.1 [45], D_i is the density diffusion term taken from Fourtakas and co-workers [46] and c^F is the fluid speed of sound. The fluid speed of sound c^F is introduced in the framework of WCSPH as the modelled fluid (or artificial fluid [11]) is approximated as more compressible than the actual fluid. To ensure that the fluid density fluctuation is kept below 1% of the initial fluid density ρ^F, c^F should be at least $10\|\mathbf{v}_{\max}\|$ where $\|\mathbf{v}_{\max}\|$ is the anticipated maximum flow speed as the density variation is proportional to the square of Mach number [11].

The force vector acting on fluid particle i can be further expanded as:

$$\mathbf{F}_i = \mathbf{F}_{P,i} + \mathbf{F}_{V,i} + \mathbf{F}_{ext,i}. \tag{13}$$

Here, $\mathbf{F}_{P,i}$ is the force generated by pressure gradient:

$$\mathbf{F}_{P,i} = -\sum_j V_i V_j (P_i + P_j) \nabla_i W_{ij}. \tag{14}$$

In WCSPH, the pressure of a liquid particle i, P_i such as water can be determined explicitly from the density ρ_i using the Tait's equation of state:

$$P_i = \frac{\rho^F (c^F)^2}{\gamma} \left(\left(\frac{\rho_i}{\rho^F} \right)^\gamma - 1 \right), \tag{15}$$

where $\gamma = 7$ [11,47] is the polytrophic index and ρ^F is the initial fluid density. For inviscid fluid modelling using SPH, the artificial viscosity term is normally added for numerical stability purpose:

$$\mathbf{F}_{V,i} = \sum_j m_i m_j \alpha h c^F \frac{(\mathbf{v}_i - \mathbf{v}_j) \bullet \mathbf{r}_{ij}}{\rho_{ij} (\|\mathbf{r}_{ij}\|^2 + 0.01 h^2)} \nabla_i W_{ij} \tag{16}$$

where α is a numerical tuning parameter and $\rho_{ij} = 0.5(\rho_i + \rho_j)$. For real viscous fluid modelling, the viscous force $\mathbf{F}_{V,i}$ can be expressed as:

$$\mathbf{F}_{V,i} = \sum_j m_i m_j \frac{4\nu^F}{\rho_i + \rho_j} \frac{\nabla_i W_{ij} \cdot \mathbf{r}_{ij}}{(\|\mathbf{r}_{ij}\|^2 + 0.01 h^2)} (\mathbf{v}_i - \mathbf{v}_j) + \sum_j m_i m_j \left(\frac{\bar{\bar{\tau}}_i}{\rho_i^2} + \frac{\bar{\bar{\tau}}_j}{\rho_j^2} \right) \nabla_i W_{ij}. \tag{17}$$

The laminar and turbulent viscous forces are represented as the first and the second summation terms appearing in the R.H.S. of Eq. (17), respectively. Here, ν^F is the fluid kinematic viscosity. The turbulent stress tensor $\bar{\bar{\tau}}$ is modelled using the Large Eddy Simulation (LES) approach [48]. For details on the SPH discretization, interested readers are referred to [49]. In the current work, unless otherwise mentioned, the flow viscous term is modelled using Eq. (17).

Any forces other than pressure and viscous forces are grouped in the external force term $\mathbf{F}_{ext,i}$. For example, the weight of a fluid particle i can be modelled as $\mathbf{F}_{ext,i} = m_i \mathbf{g}$, where $\mathbf{g}$ is the gravitational acceleration vector.

2.3. Fluid-structure coupling

For modelling the wall boundary conditions at the fluid–solid interface, the solid particles near the fluid–solid interface are treated as dummy particles in the support domain of SPH particle. Here, the Dynamic Boundary Condition (DBC) approach [50] is adopted to compute the pressure of dummy/solid particle I, P_I. Following this, the pressure and viscous forces (from fluid and turbulent viscosities) acting on a fluid particle i due to a neighboring solid particle I can be determined as:

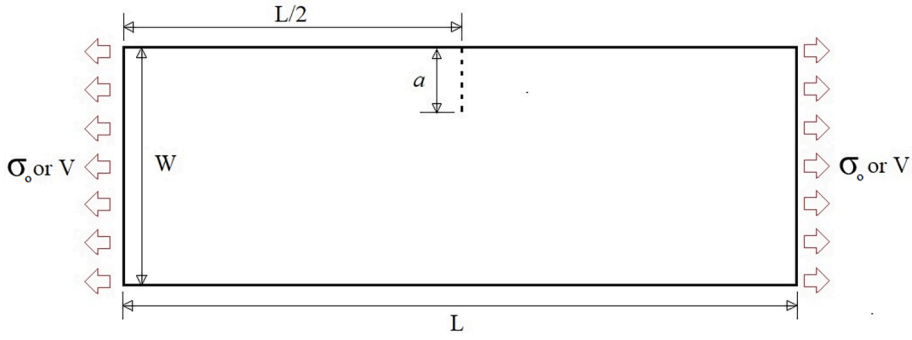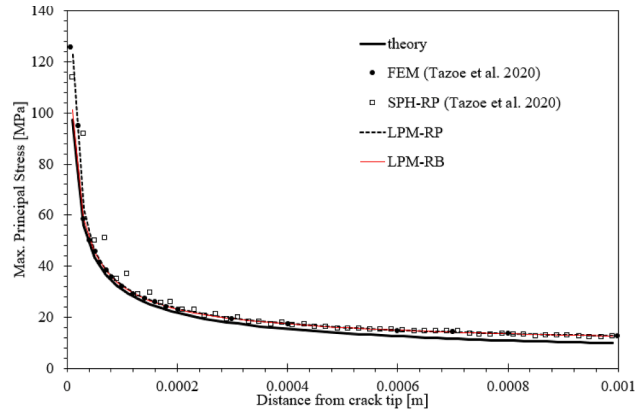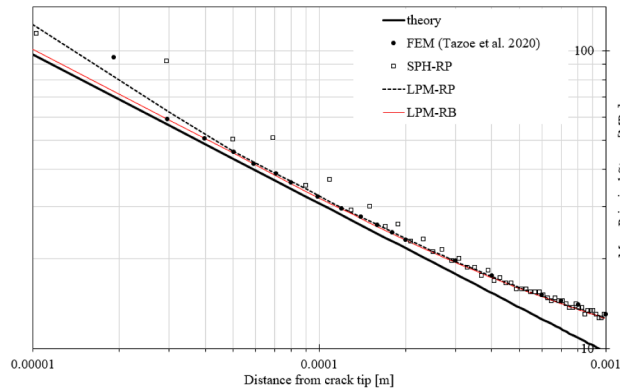$$\mathbf{F}_{P,I \to i} = -V_i V_I (P_i + P_I) \nabla_i W_{iI} \tag{18}$$

and

Fig. 3. Geometry of the 2D plate with an initial edge-crack line of length a. The side edges are subjected to either stress (σ_o) or velocity (V) boundary conditions.

(a)

(b)

Fig. 4. Stress distribution with respect to the distance from the crack tip ($\theta = 0^o$). (a) Normal scale; (b) Logarithmic scale. The particle spacings for SPH [32] and LPM are $D_p = 0.02$ mm.

$$\mathbf{F}_{V,I \to i} = m_i m_I \frac{4\nu^F}{\rho_i + \rho_I} \frac{\nabla_i W_{iI} \cdot \mathbf{r}_{iI}}{\left(\|\mathbf{r}_{iI}\|^2 + 0.01h^2 \right)} (\mathbf{v}_i - \mathbf{v}_I) + m_i m_I \left(\frac{\bar{\bar{\tau}}_i}{\rho_i^2} + \frac{\bar{\bar{\tau}}_I}{\rho_I^2} \right) \nabla_i W_{iI} \tag{19}$$

respectively. The dummy particle density ρ_I is calculated using the DBC approach [50], whereas the dummy particle volume, V_I is computed as $V_I = \frac{m_i}{\rho_I}$. Here, m_i is the mass of an interacting fluid particle. Note that the solid particle I is treated as the dummy particle of an interacting fluid particle i; hence, its mass, m_I in Eq. (19) is taken as $m_I = m_i$. Finally, the total hydrodynamic force acting on a solid particle I, $\mathbf{F}_{F \to S,I}$ (see Eq. (1)) can then be computed:
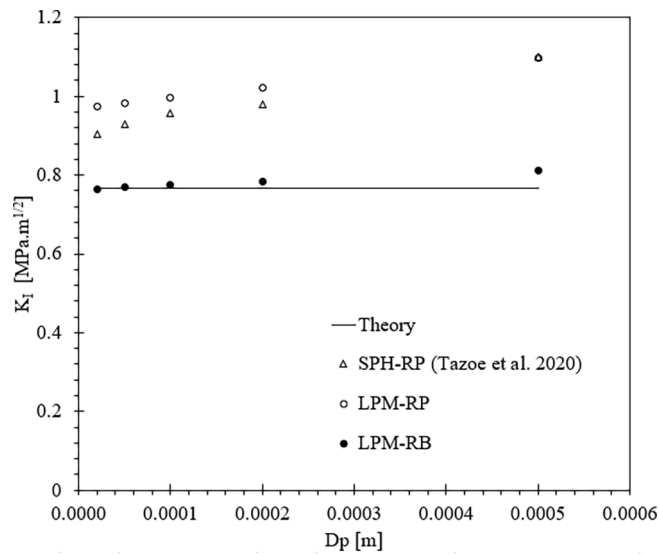
Fig. 5. Spatial convergence of K_I using different methods. The theoretical value K_I is 0.766 MPa.m$^{1/2}$.
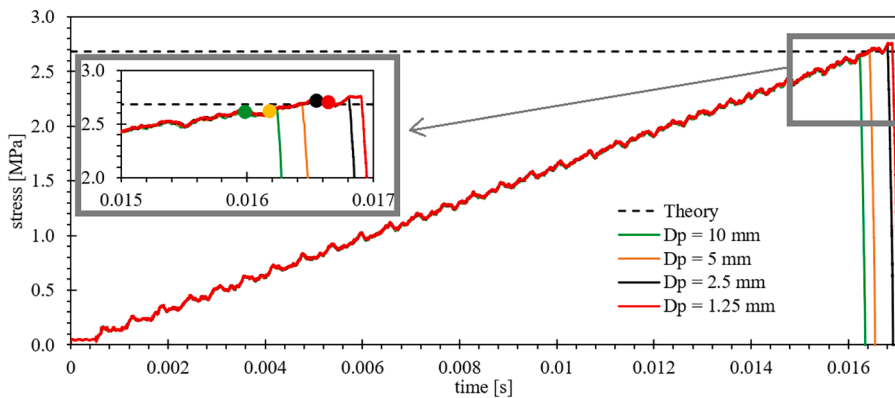

Fig. 6. Convergence of the peak far-field stress at the right edge of the plate (with an initial crack line at the edge) due to brittle fracture. Solid data points in the close-up view indicates the respective far-field stress and the time instant when the first fracture near the crack tip is detected.
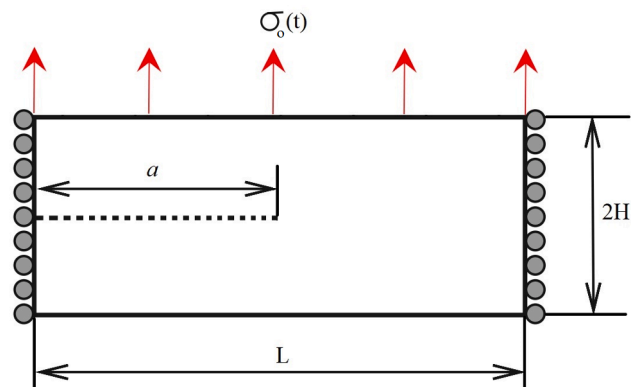

Fig. 7. A semi-infinite plate of $L = 10$ m and $H = 2$ m with an initial crack of length $a = 5$ m subjected to a time-varying tensile stress applied at the top edge.
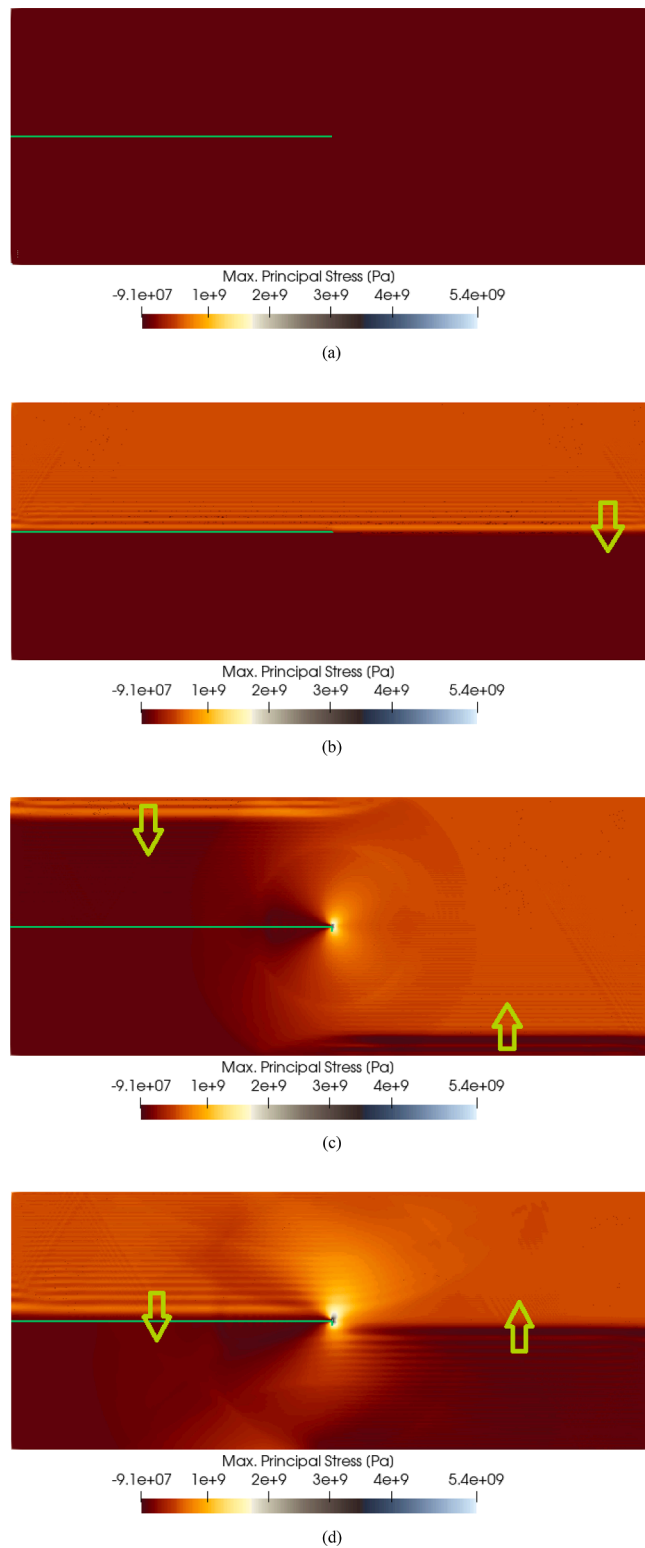
Fig. 8. Propagation of tensile stress wave (arrow indicates its direction) under step tensile loading (top edge) at $t =$ (a) 0 s; (b) 3.4×10^{-4} s ($= t_c$), (b) 7.3×10^{-4} s ($= 2.13t_c$); and (d) 1.0×10^{-3} s ($= 3t_c$). The green line indicates the initial crack line.
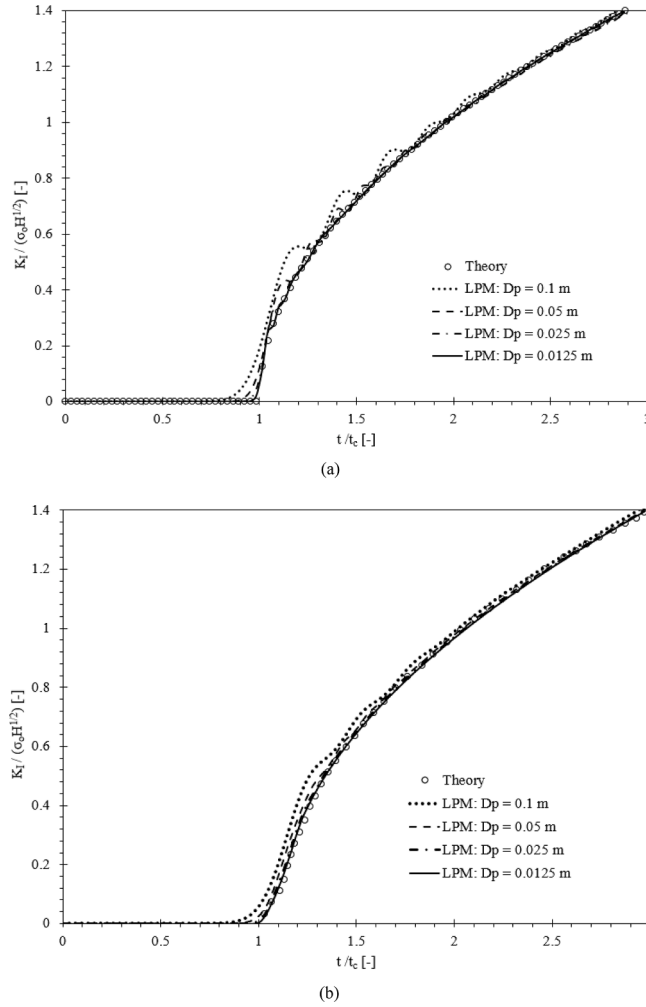
(a)

(b)

Fig. 9. Time history of the normalized stress intensity factor for various particle spacings simulated using LPM. Different $\sigma_o(t)$ profiles are used: (a) Step profile; (b) Ramp profile. Time is normalized using $t_c = H/c_1$.

$$\mathbf{F}_{F \to S,I} = -\sum_{i \in N_f} \left(\mathbf{F}_{P,I \to i} + \mathbf{F}_{V,I \to i} \right) \qquad (20)$$

Here, N_f is the number of fluid particles in the support domain of solid particle I.

By incorporating the explicit predictor–corrector approach, both equations of motion of fluid and solid bodies are integrated in a staggered manner for fluid–structure coupling [51]. As the maximum allowable time step size in an explicit solid solver is generally smaller than that of a fluid solver, the equations of motion of solid bodies are integrated multiple times to achieve time synchronization with the fluid body. Interested readers are referred to our previous works for further details [34,51].

3. Results and discussion

In this section, the brittle fracture model incorporated in the LPM method is validated first for pure solid mechanics problems. In particular, the accuracy and convergence of the mode-I Stress Intensity Factor (SIF) formula proposed in the current work (Eq. (6)) are investigated for both static and dynamic loading conditions by comparing the numerical results against the theoretical solutions of a series of benchmark test cases. The dynamic crack branching problem is then studied, and the result is validated by using the experimental and FEM data. Finally, the capability of the current SPH-LPM method in simulating FSI problems involving solid fracture is demonstrated. Unless otherwise specified, plane strain condition is assumed for all the 2D solid models.
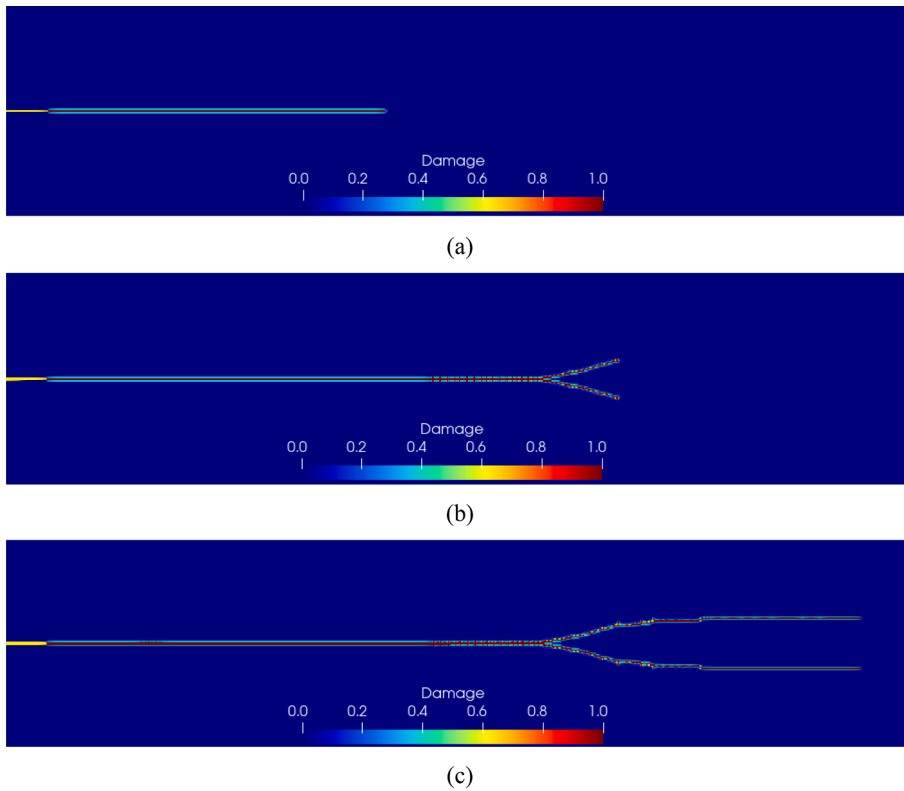
Fig. 10. Crack propagation from the notch on the left and damage evolution at $t =$ (a) 28 µs; (b) 36 µs and (c) 48 µs predicted using LPM. $D_p =$ 0.0625 mm.
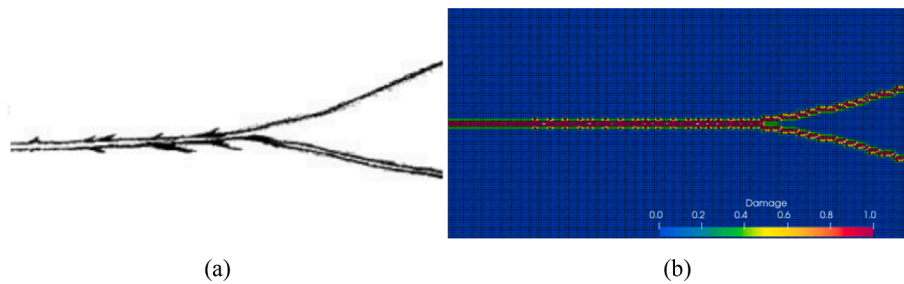

Fig. 11. Comparison of the crack path: (a) experimental observation [56] and (b) simulation using the current LPM method ($D_p =$ 0.0625 mm).

3.1. Static loading

3.1.1. Stress intensity factor

This test case was previously simulated by Tazoe and co-workers [32,33] using SPH to investigate the accuracy of their Mode-I SIF formulation (Eq. (5)). The plate is made of low carbon steel JIS-S50C with material properties [52]: $E = 210$ GPa; $v^S = 0.3$; $\rho^S = 7800$ kg.m^{-3}. The geometry layout is shown in Fig. 3, with $W = 5$ mm, $L = 8$ mm and $a = 1$ mm. Both left and right ends are subjected to a constant tensile stress $\sigma_o = 10$ MPa.

Fig. 4 shows the stress value as a function of displacement from the crack tip ($\theta = 0^o$). Although the SPH solutions of Tazoe and co-workers [32] exhibit unphysical wiggles near the crack tip, the SPH solutions are in general trending quite well with the theoretical solution. Here, for $\theta = 0^o$, the theoretical stress value as a function of distance from the crack tip (r) is computed as:

$$\sigma(r) = \frac{K_{I,theo}}{\sqrt{2\pi r}}, \tag{21}$$

which is valid only near the crack tip. For this plate geometry and initial crack configuration, the theoretical value of K_I, i.e. $K_{I,theo}$ can be determined as [41]:
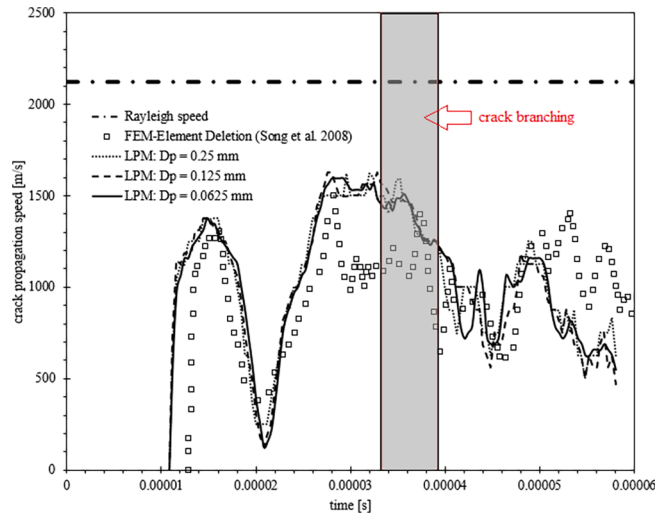
Fig. 12. Comparison of crack tip propagation speeds using LPM and FEM-Element Deletion method [55]. No crack branching was detected when FEM-Element Deletion method was used.
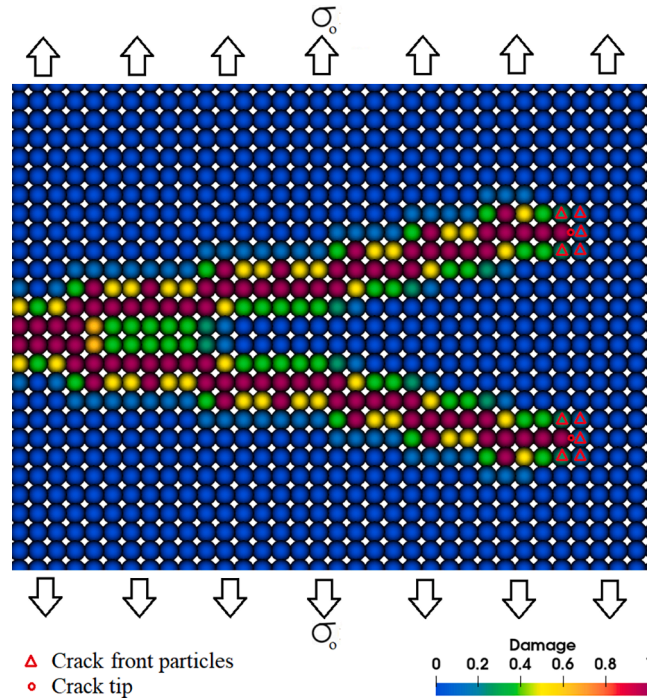

Fig. 13. Potential crack front particles during crack branching at $t = 34.4$ μs.

$$K_{I,theo} = \sigma_o \sqrt{\pi a} \; \frac{\sqrt{\frac{2W}{\pi a} \tan \frac{\pi a}{2W}} \left[0.752 + 2.02 \frac{a}{W} + 0.37 \left(1 - \sin \frac{\pi a}{2W} \right)^3 \right]}{\cos \frac{\pi a}{2W}}, \tag{22}$$

which turns out as $K_{I,theo} = 0.766$ MPa.m$^{1/2}$. It is important to note that the accuracy of Eq. (22) is 0.5 % for any value of a/W. In general, by modelling the initial crack line via particle removal method (RP method), the SPH-RP [32] and the current LPM-RP methods overpredict the stress value near the crack tip. The near-tip stress value predicted using FEM [32] is higher than the theoretical solution as well. At locations further away from the crack tip, the predicted stresses using FEM, SPH and LPM are almost indiscernible and apparent discrepancies against the theoretical solution can be found at these locations. Nonetheless, it is important to note that the theoretical stress formula (Eq. (21)) is no longer valid at locations far from the crack tip.
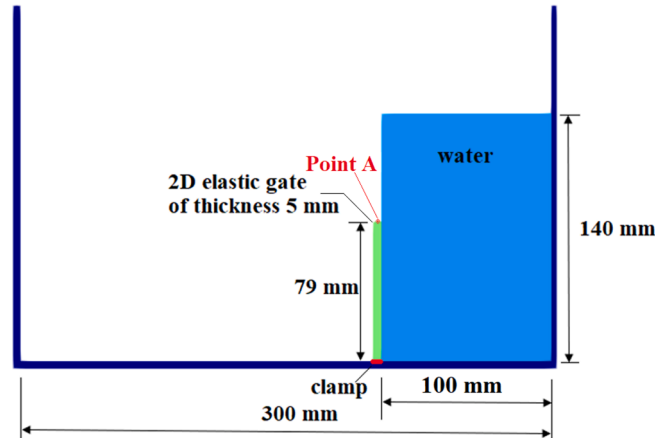
Fig. 14. Geometric configuration of 2D elastic gate (clamped at the bottom). Point A is located at the middle of the gate's tip.

Next, by modelling the initial edge-crack line via removing the bonds of respective LPM particles (LPM-RB), it is found that the predicted near-tip stress value is quite close to the theoretical solution. The spatial convergence tests of LPM and SPH in predicting the mode-I Stress Intensity Factor, K_I are then carried out and the results are shown in Fig. 5. In general, the numerical errors of SPH and LPM methods decrease with respect to the particle size; however, the errors of SPH-RP [32] and LPM-RP methods are still quite apparent even when a fine particle size ($D_p = 0.02$ mm) is used. For LPM-RB, it is encouraging to note that the predicted K_I values compare quite well with the theoretical solution as the particle resolution is refined. At $D_p = 0.02$ mm, the computed K_I value using LPM-RB (Eq. (6)) is 0.764 MPa.m$^{1/2}$ (~0.26% difference as compared to $K_{I,theo} = 0.766$ MPa.m$^{1/2}$).

In the following test cases, the LPM-RB method will be adopted, and the acronym LPM-RB will be replaced by LPM for brevity purpose.

3.1.2. Failure load

From the Linear Elastic Fracture Mechanics (LEFM) theory, for a plate with a sufficiently long initial edge crack as illustrated in Fig. 3, it might fail due to brittle fracture if the applied far-field stress σ_o is larger than the critical stress:

$$\sigma_{o,crit} = \frac{K_{I,C}}{\sqrt{\pi a}} \left[\frac{\sqrt{\frac{2W}{\pi a} tan\frac{\pi a}{2W}} \left[0.752 + 2.02\frac{a}{W} + 0.37\left(1 - sin\frac{\pi a}{2W}\right)^3 \right]}{cos\frac{\pi a}{2W}} \right]^{-1}, \quad (23)$$

where $K_{I,C}$ is the fracture toughness of a material.

The geometrical description of this test case is outlined in Fig. 3, with $W = 0.25$ m, $L = 2.0$ m, and $a = 0.03$ m. Following Tavarez and Plesha [30], the material properties are set as: $E = 29.7$ GPa; $v^S = 0.3$; $\rho^S = 2700$ kg.m^{-3}; $\sigma_{UTS} = 3.44$ MPa and $K_{I,C} = 1.0$ MPa.m$^{1/2}$. A small constant velocity of 5 mm/s is imposed on the left and right edges of the plate to model the quasi-static state. This constant velocity is chosen as it is found that the peak far-field stress causing complete failure is almost similar to that simulated using a smaller constant speed of 2.5 mm/s.

Fig. 6 compares the time histories of far-field stresses at the right edge of the plate subjected to tension (see the plate model in Fig. 3). As seen, when the particle resolution is refined, the simulated $\sigma_{o,crit}$ leading to the first detection of fracture approaches to the theoretical value. Beyond this juncture, the crack would propagate unstably until complete failure occurs in the plate model, which is witnessed by the sudden drop of far-field stress in Fig. 6.

3.2. Dynamic stress intensity factor

Having tested the numerical accuracy and numerical convergence of Eq. (6) for static loading case, the test case involving a dynamic stress boundary condition is considered in this section. The main intention is to test the accuracy of Eq. (6) in predicting the dynamic Mode-I SIF near the crack tip. Fig. 7 shows a plate with an initial crack of length subjected to a time-varying tensile stress at the top. Here, we intend to study the time evolution of mode-I stress intensity factor K_I near the crack tip upon applying the time-varying tensile stress from the top. Two temporal profiles of applied tensile stresses are tested, which are the step loading profile:

$$\sigma_o(t) = \begin{cases} 0 & t < 0 \\ \sigma^* & t \geq 0 \end{cases}, \quad (24)$$
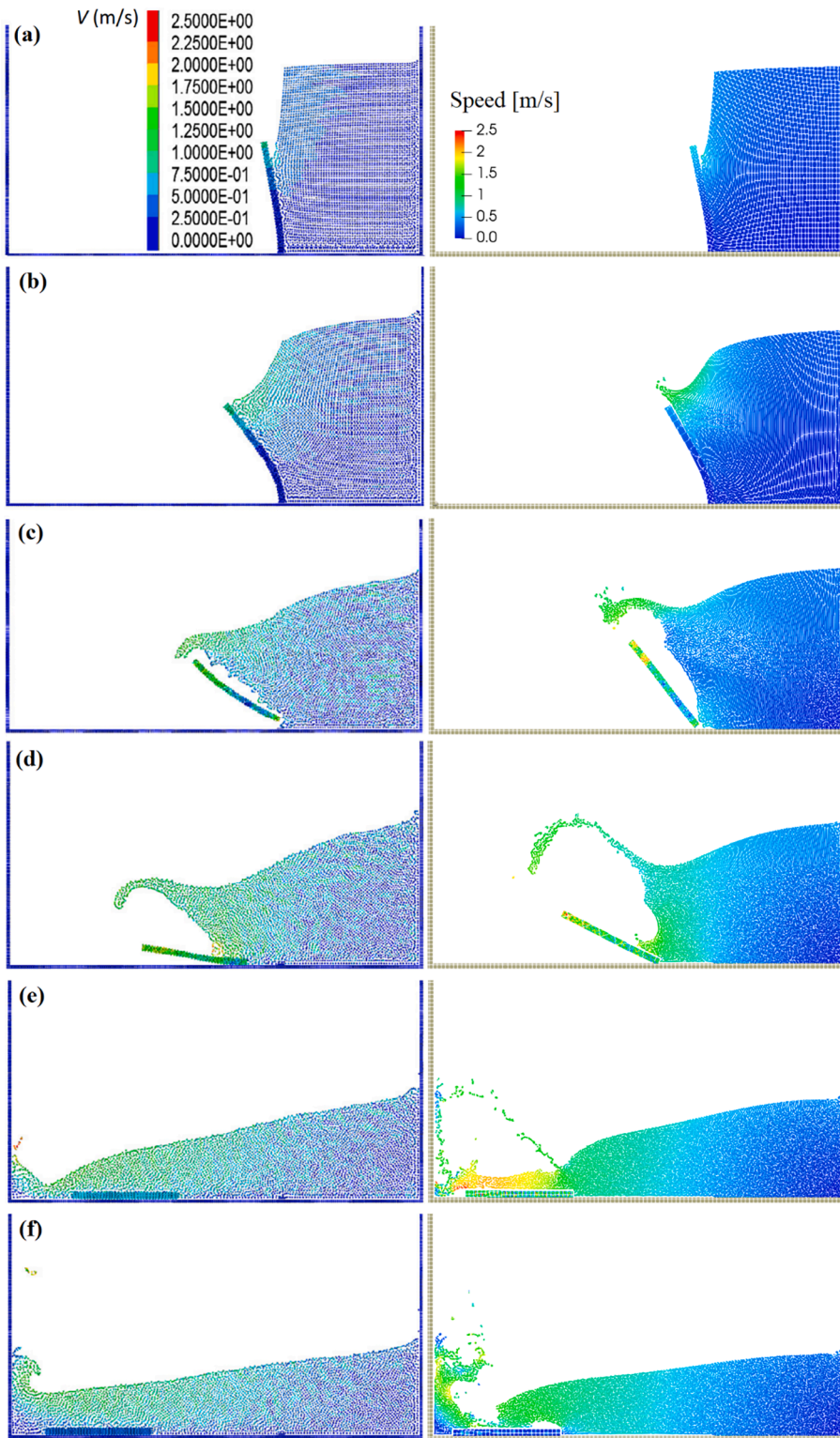
and the ramp loading profile:

Fig. 15. Fracturing of elastic plate due to dam breaking at (a) t = 0.04 s; (b) t = 0.08 s; (c) t = 0.12 s; (d) t = 0.16 s; (e) t = 0.24 s; (f) t = 0.28 s. Left: SPH-DEM [23]; Right: current 2D SPH-LPM.
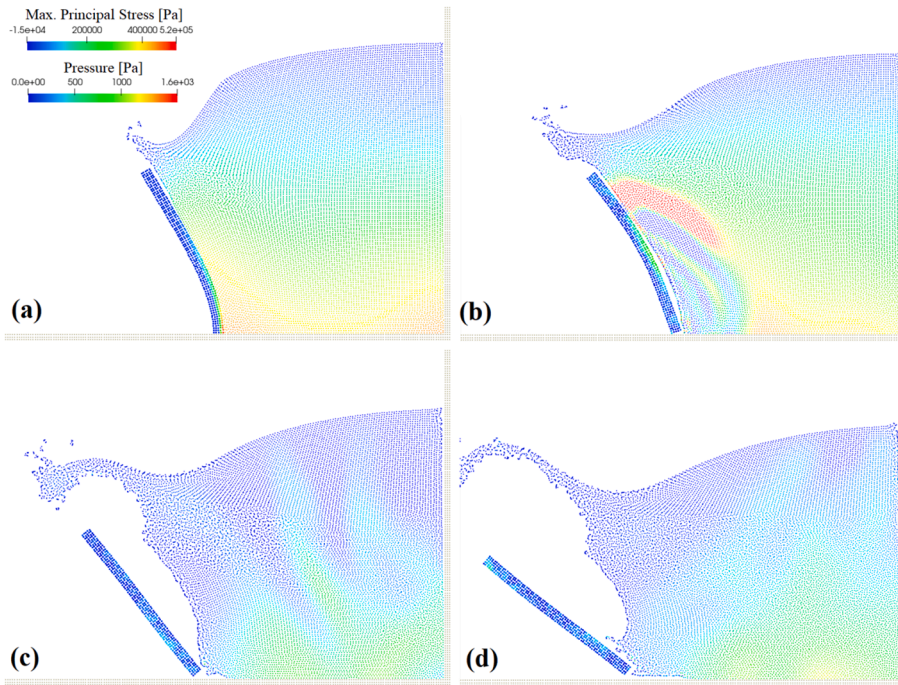
Fig. 16. Close-up views of the fluid pressure and solid maximum principal stress at $t =$ (a) 0.08 s; (b) 0.10 s; (c) 0.12 s and (d) 0.14 s.
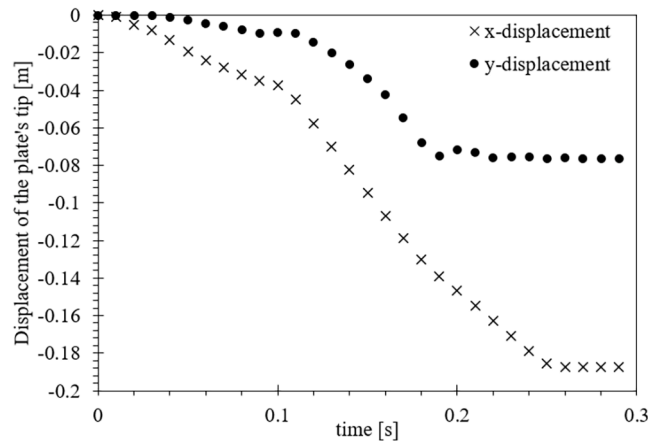

Fig. 17. Displacement of the plate's tip (Point A).

$$\sigma_o(t) = \begin{cases} 0 & t < 0 \\ 5\sigma^* \dfrac{t}{t_c} & t \geq 0 \end{cases}.$$ (25)

where $\sigma^* = 500$ MPa [53]. The critical time t_c is defined as $t_c = H/c_1$, where $H = 2$ m (see Fig. 7) and $c_1 = 5944$ m/s is the dilatational speed [53]. Following [53], the material properties are set as: $E = 210$ GPa; $v^S = 0.3$; $\rho^S = 8000$ kg.m^{-3}.

If the crack shown in Fig. 7 exists in an infinite domain, an analytical solution on the time variation of K_I near the crack tip is available [54]. However, since the current plate model is finite in size, the simulation is stopped at $t = 3t_c$, i.e. the instant when the reflected wave from the bottom edge hits the crack tip [53,54]. Beyond $t = 3t_c$, the analytical solution is no longer valid. Fig. 8 shows the travelling of stress wave simulated using the current LPM method and Fig. 8(d) clearly shows the reflected stress wave hits the crack tip from the bottom at $t = 3t_c$.

The K_I value of the crack front particle obtained from Eq. (6) is normalized using $\sigma^* \sqrt{H}$ and the result is plotted in Fig. 9 in the normalized time (t/t_c) domain. For cases simulated using coarser particle resolution, it is observed that the numerical oscillation for the step loading case is more apparent than that for the ramp loading one. It could be due to the ramp loading profile which is less abrupt
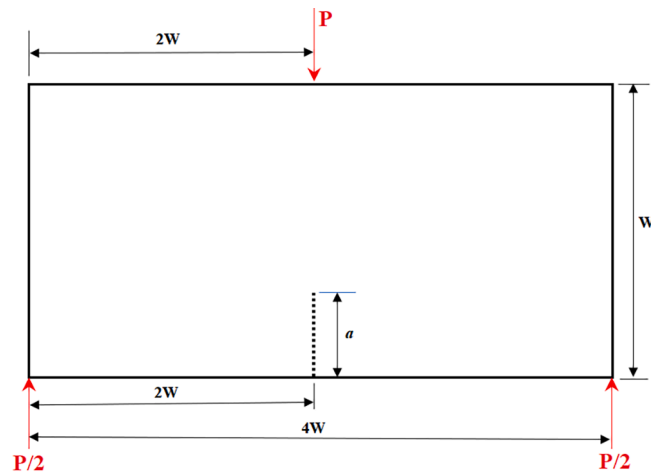
Fig. 18. 2D Single-edge notch-bending specimen of width $W = 0.04$ m and initial crack length $a = 0.01$ m subjected to force $P = 0.02$ N at the top. The thickness of the specimen is assumed as $B = 1.0$ m.
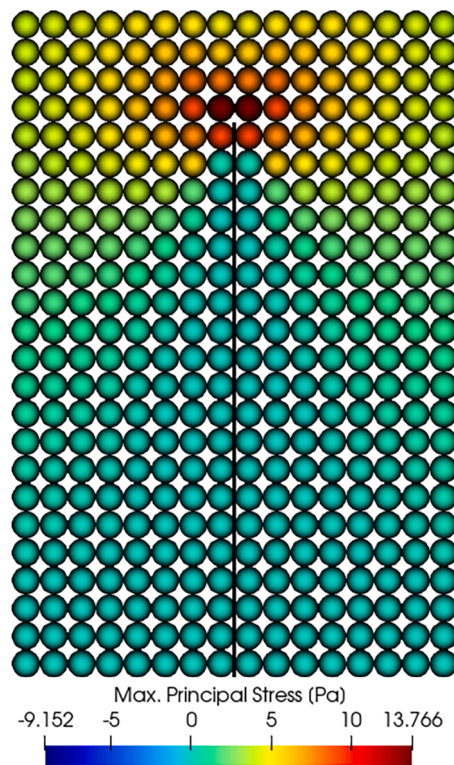

Fig. 19. Maximum principal stress near the crack tip for the single-edge notch-bending test at equilibrium condition. $D_p = 0.5$ mm. Black solid line indicates the initial crack line.

(smoother) than the step loading profile. For both loading conditions, the numerical error is more apparent at $t = t_c$ when the stress wave first hits the crack tip (see Fig. 8 (b)). As shown in Fig. 9, by employing finer particle resolution, the numerical oscillation is suppressed, and the result converges to the analytical solution.

3.3. Dynamic crack branching

Having verified the accuracy of SIF computation, the next task is to apply the failure criterion in simulating crack propagation problem. This case involves crack propagation in a rectangular plate with an initial crack line as outlined in Fig. 3, with $W = 0.1$ m, $L =$
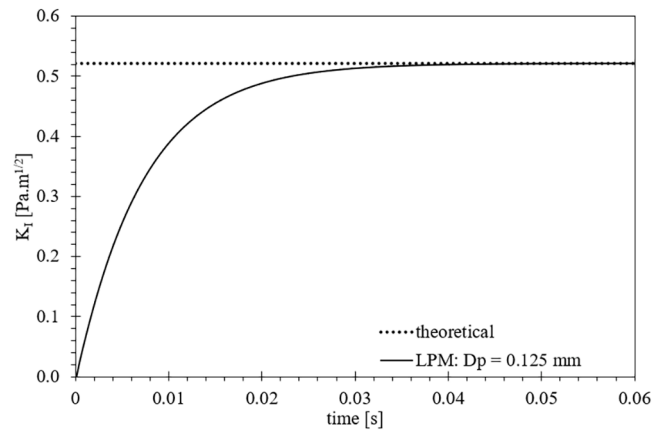
Fig. 20. Comparison of K_I values for the single-edge notch-bending test. The theoretical K_I value is 0.522 Pa.m$^{1/2}$.

Table 1
Computed Mode-I stress intensity factor (K_I) for the single-edge notch-bending test using different LPM particle sizes.

Particle size [mm]	K_I[Pa.m$^{1/2}$]
1.0	0.5157
0.5	0.5191
0.25	0.5204
0.125	0.5209

Fig. 21. Geometric configuration of the case consisting of a water column of height = 140 mm and width = 100 mm resting on a flexible plate of height = 4 mm. A vertical initial crack line (red colour) of length = 1.8 mm is located at the middle of the flexible plate. (For interpretation of the references to colour in this figure legend, the reader is referred to the web version of this article.)

0.04 m and $a = 0.05$ m. By using LPM, this problem has been studied by Chen and co-workers using triangular LPM lattice and the critical force criterion [29]. In this study, we model it using square lattice to be consistent with the discretization used in SPH for simulating fluid problems later. The plate is subjected to a tensile stress of $\sigma_o = 1$ MPa applied at the left and right edges. The material properties of the rectangular plate are: Young's modulus $E = 32$ GPa, Poisson ratio $v^S = 0.2$ and solid density $\rho^S = 2450$ kg.m^{-3}. The material ultimate tensile strength σ_{UTS} and fracture toughness $K_{I,C}$ are taken as 12 MPa [29] and 0.316 MPa.m$^{1/2}$ (consistent with
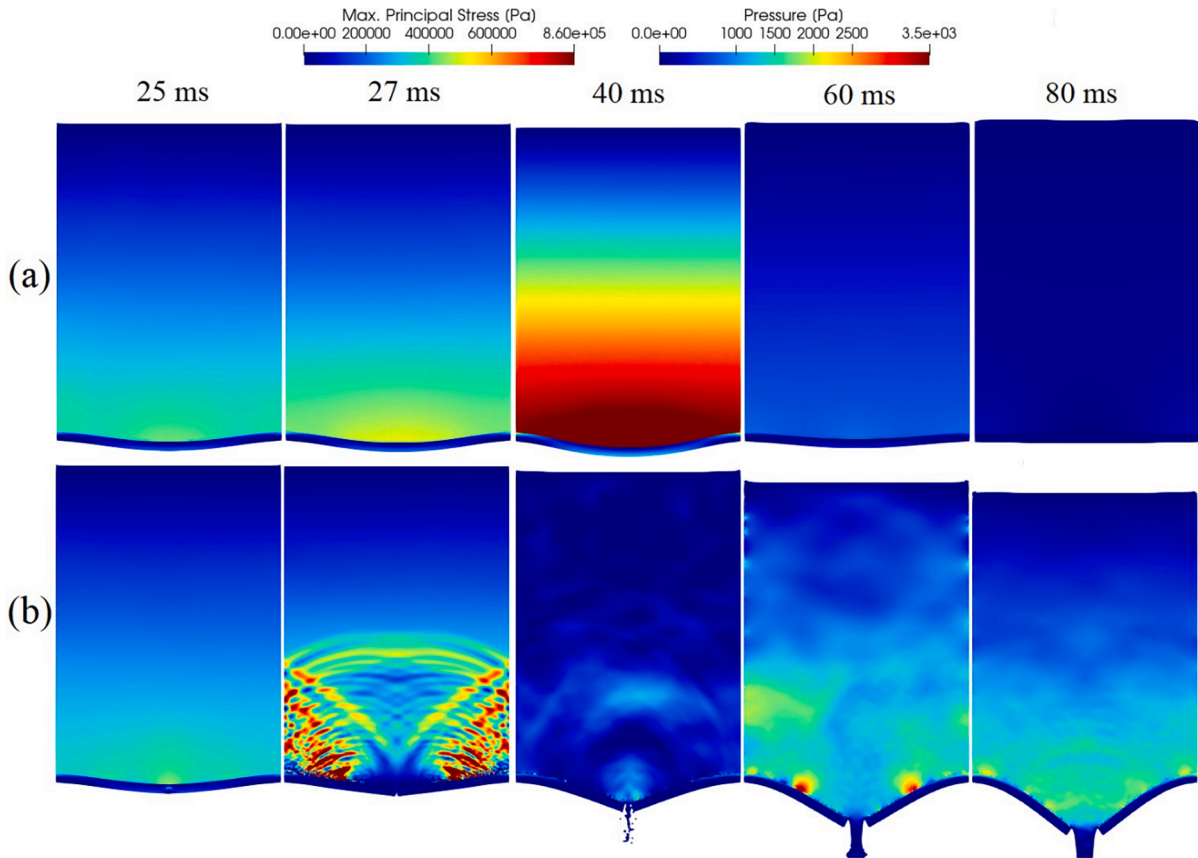
Fig. 22. Fluid pressure and solid maximum principal stress at different time frames for cases involving (a) no initial crack; (b) a vertical initial crack at the bottom of the plate.

fracture energy of 3 J.m^{-2} [55]).

As shown in Fig. 10, the main crack propagates from the initial crack tip and branches into two oblique cracks subsequently and these new cracks propagate further in different directions. This is consistent with the experimental observation [56] as reported in Fig. 11. From the experimental photo (Fig. 11 (a)), it is observed as well that some minor cracks are generated from the main crack before the branching point. It is appealing to note that these experimentally observed minor cracks that grow only to a small length, which are completely missing in the previous XFEM prediction [55], are somewhat captured in our current numerical simulation (see Fig. 11 (b)).

Fig. 12 compares the crack tip speeds predicted using different methods. It is found that the current LPM method shows marginal amount of particle size dependence in the crack tip speed. From the LPM results, the crack starts to propagate from the initial crack tip at $t \sim 11$ μs. The crack speed increases and bottoms at $t \sim 21$ μs, which is consistent with that simulated using FEM via the element deletion method [55]. The reason of this plunge in crack tip speed is unclear and it is worth further investigation in the future. The crack tip speed predicted using LPM rises to $v_{tip} \sim 1500$ ms^{-1} and it plateaus for around 5 μs before branching occurs (still below the Rayleigh speed) at around $t_{banching} = 33$ μs (cf. $v_{tip} \sim 1500$ ms^{-1} at $t_{banching} \sim 30.2$ μs predicted using cracking node method [57]). Upon branching, the crack propagation speed decreases, consistent to that reported by Bowden and co-workers [58]. On the other hand, branching does not occur when the element deletion method [55] is employed in FEM, which could be due to its relatively low predicted crack tip speed and hence branching cannot be triggered.

The potential crack front particles in front of the crack tip during crack branching are shown in Fig. 13. As mentioned in Section 2.1.1, strictly speaking, the pure mode-I SIF formula in Eq. (6) is no longer applicable during crack branching, as the crack line is not perpendicular to the external loading direction as shown in Fig. 13. For more accurate computation of the SIF values of these crack front particles, the R.H.S. of Eq. (4) should be modified [41] to include both Mode-I and Mode-II SIFs and this is left for future development.
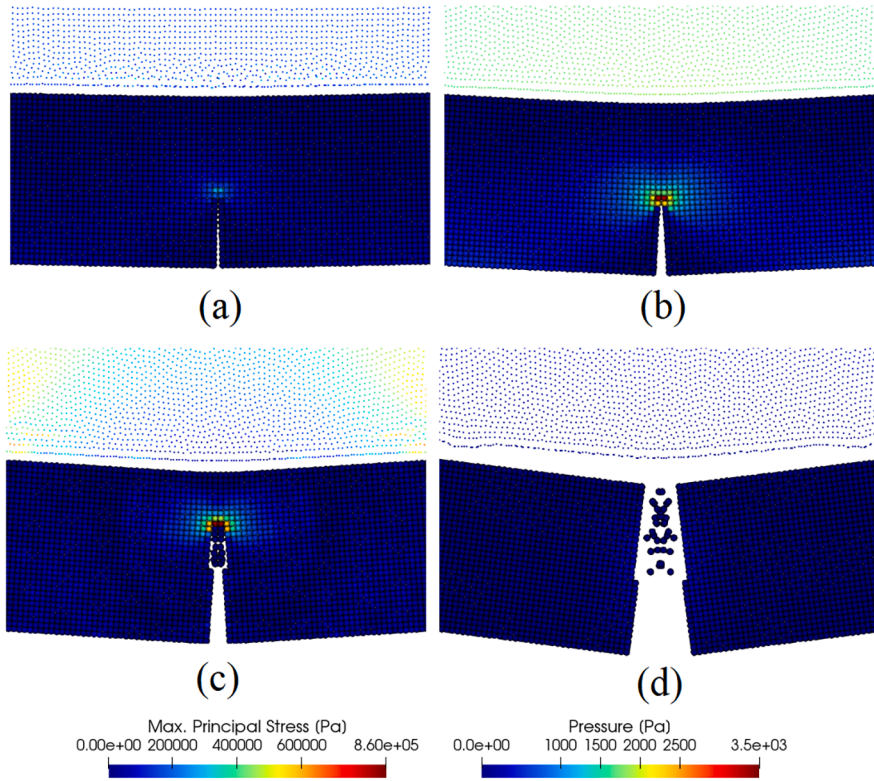
Fig. 23. Fracturing of the flexible plate subjected to fluid pressure from the top predicted using the current SPH-LPM method ($D_p = 0.125$ mm) at t = (a) 15 ms; (b) 25 ms; (c) 26 ms and (d) 27 ms.

3.4. Fluid structure interaction

3.4.1. 2D elastic gate with FSI and fracture

This 2D problem is the preliminary FSI test case involving fracture that was initially simulated by Wu and co-workers [23] using SPH-DEM method. The geometrical configuration of the test case is shown in Fig. 14. Here, 2D plane strain condition is assumed for the elastic gate. The material properties of the gate are: $E = 12$ MPa; $v^S = 0.33$; $\rho^S = 1100$ kg.m^{-3}. The material tensile strength of the gate is assumed as $\sigma_{UTS} = 0.52$ MPa, which is small enough to allow for gate fracture to occur. To compare our results against those of [23], only the Rankine failure criterion is employed. In other words, the SIF criterion is not considered here, consistent with the assumption made in [23].

The water column collapses due to gravity, and it is anticipated that the elastic gate would deform accordingly until it is detached from the bottom support if the material tensile strength is exceeded. The simulation results are compared against those of Wu and co-workers [23] in Fig. 15. The maximum principal stress of the gate is plotted as well in Fig. 16. At $t = 0.08$ s (Fig. 16 (a)), due to gate bending, the tensile stress is concentrated at the side of the gate (facing the water body). At $t = 0.12$ s, the entire gate is detached from the bottom support, and it starts to fall towards the floor level. From Fig. 15(d), the gate touches the floor at $t \sim 0.16$ s, and it slides along the floor due to the fluid force from the collapsing water column. The sliding motion stops around $t \sim 0.26$ s as the x-displacement of the plate's tip (Point A, see Fig. 14) forms a plateau at $t > 0.26$ s as shown in Fig. 17. It can be observed from Fig. 17 that the plate's tip speed experiences a sudden increase at $t \sim 0.1$ s immediately after the gate is detached from the bottom support. In general, the current SPH-LPM results compare quite well with those of Wu and co-workers [23]. The discrepancies between the two results are more noticeable upon the failure of the elastic gate which could be due to different numerical settings in both SPH FSI solvers.

In the current simulation, it is noticed that the elastic gate would penetrate through the floor if no collision modelling is considered. To address this problem, the pin-ball collision model [59,60] is employed when penetration occurs between two solid particles (or $p > 0$), where $p = Dp - \|\mathbf{r}_J - \mathbf{r}_I\|$ is the penetration distance. If penetration occurs, the collision force $\mathbf{F}_{C,I}$ is added to $\mathbf{F}_{ext,I}$ in Eq. (1) as:

$$\mathbf{F}_{C,I} = K \bullet \min(F_1, F_2)(\mathbf{r}_I - \mathbf{r}_J)\big/\|\mathbf{r}_I - \mathbf{r}_J\|, \tag{26}$$
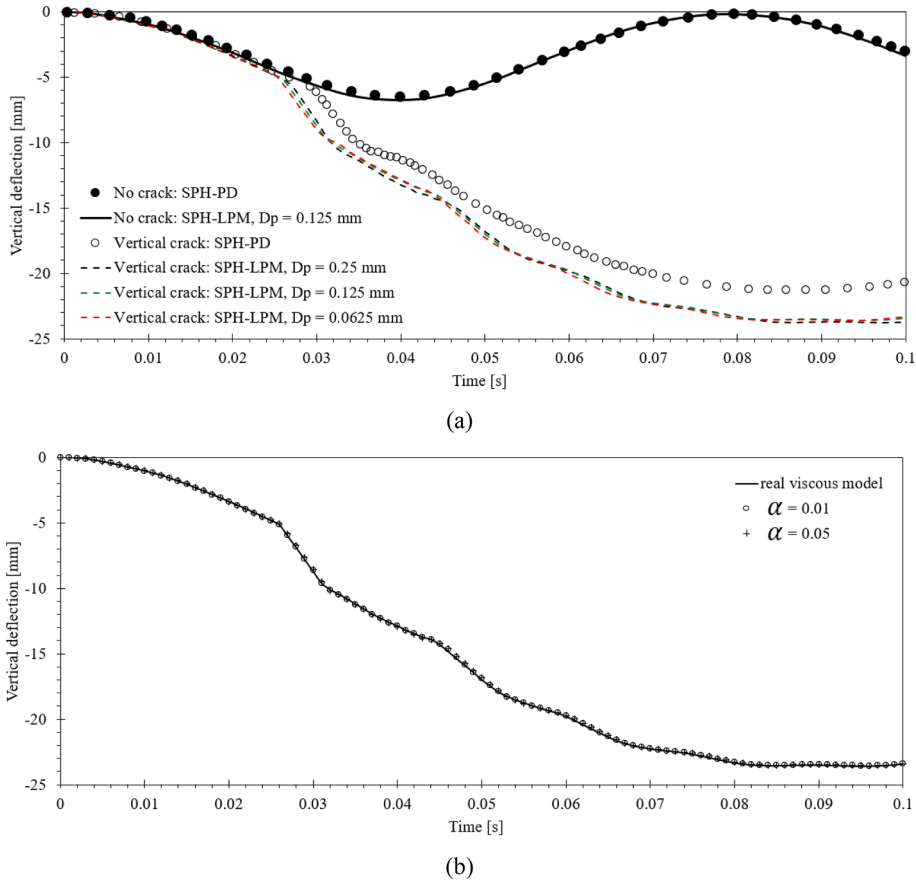
where

Fig. 24. Simulated vertical deflections at the middle lower point of the flexible plate. (a) Sensitivity of particle resolution. For SPH-PD [22], the solid particle spacing is 0.125 mm, and the fluid particle is 1 mm; (b) Sensitivity of viscous model. $D_p = 0.125$ mm.

$$F_1 = \begin{cases} \dfrac{\rho_I \rho_J R_I^3 R_J^3}{\rho_I R_I^3 + \rho_J R_J^3} \dfrac{\dot{p}}{\Delta t} & \dot{p} > 0 \\ 0 & \dot{p} \leq 0 \end{cases}, \tag{27}$$

$$F_2 = \left[\frac{G_I G_J}{G_I + G_J} \sqrt{\frac{R_I R_J}{R_I + R_J}} \right] p^{1.5}, \tag{28}$$

$$\dot{p} = (\mathbf{v}_I - \mathbf{v}_J) \bullet \frac{(\mathbf{r}_J - \mathbf{r}_I)}{\|\mathbf{r}_J - \mathbf{r}_I\|}. \tag{29}$$

Here, R_I is the radius of solid particle I taken as $0.5D_p$, ρ_I and G_I are density and shear modulus of solid particle I, respectively. It should be noted that the collision force is applied between non-bonded solid particles (appeared on newly formed crack surfaces) and solid-wall particles only. The parameter K is case-dependent, and it needs to be tuned. In the current simulation, K is set as 1200. Indeed, a tuning-free collision model is necessary to ensure the robustness of the current method. Nevertheless, this is not within the scope of the current work.

3.4.2. Fracture due to hydrostatic fluid pressure

3.4.2.1. 2D Single-edge notch-bending test. Before the recent FSI test case of Rahimi and co-workers [22] involving brittle fracture of a flexible plate (clamped at both ends) due to hydrostatic fluid pressure acting from the top is studied, a similar solid mechanics case involving a single-edge notch-bending specimen subjected to a concentrated force acting from the top is simulated first. Here, we intend to compute the K_I value near the crack tip and make comparison against the theoretical solution. Fig. 18 shows the geometrical details of this test case. For this case, the theoretical solution of K_I is available [61]:
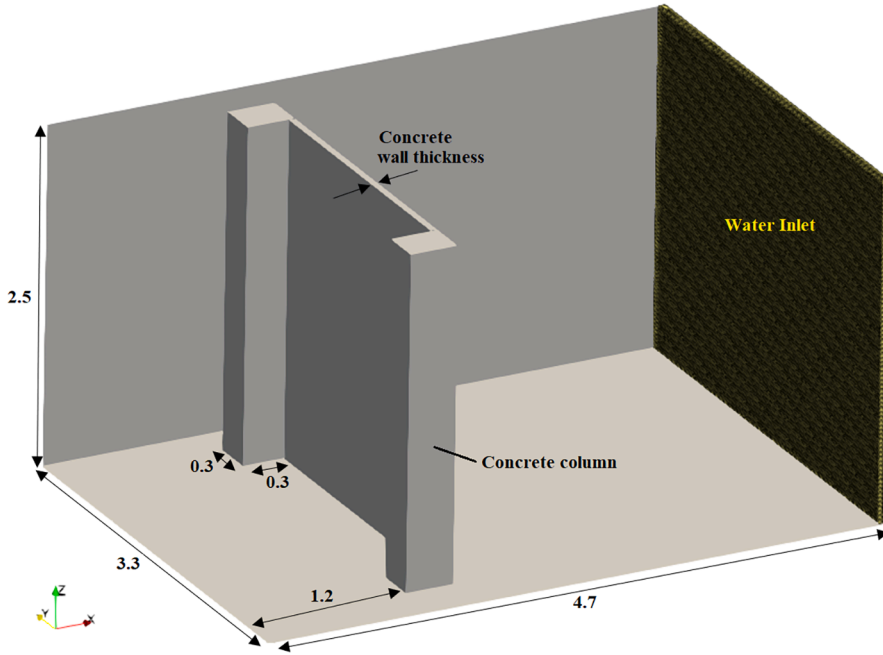
Fig. 25. Geometry configuration of the concrete wall and concrete column subjected to tsunami from the right. The height of concrete column is same as that of the problem domain. All dimensions are in meter [m].

$$K_{I,theo} = \frac{4P}{B}\sqrt{\frac{\pi}{W}}\left[1.6\left(\frac{a}{W}\right)^{1/2} - 2.6\left(\frac{a}{W}\right)^{3/2} + 12.3\left(\frac{a}{W}\right)^{5/2} - 21.2\left(\frac{a}{W}\right)^{7/2} + 21.8\left(\frac{a}{W}\right)^{9/2}\right],$$ (30)

where $P = 0.02$ N is the applied force, $a = 0.01$ m is the initial crack length, $W = 0.04$ m is the specimen width and $B = 1.0$ m is the specimen thickness. Based on the above data, $K_{I,theo} = 0.522$ Pa.m$^{1/2}$. Next, the K_I value of the crack front particle where the maximum principal stress is the highest (see Fig. 19) is computed. As shown in Fig. 20, by using $D_p = 0.125$ mm, the predicted K_I value approaches to the theoretical solution as time elapses. The sensitivity of particle resolution is investigated and the results are reported in Table 1. As seen, as the particle resolution is refined, the K_I value converges to the analytical solution.

3.4.2.2. Rahimi's FSI case. Finally, we test our method in simulating FSI problem involving brittle fracture of a flexible plate subjected to the hydrostatic water pressure acting from the top. This problem has been recently simulated by Rahimi and co-workers [22] using the SPH-Peridynamics (SPH-PD) method. Fig. 21 shows the geometrical setup of this problem, where the water density and water kinematic viscosity are taken as $\rho^F = 1000$ kg.m^{-3} and $\nu^F = 10^{-6}$ m^2/s, respectively. To be consistent with the SPH model setting of [22], the fluid speed of sound c^F is set as 60 ms^{-1}. The material properties of the flexible plate are: Young's modulus $E = 10$ MPa, Poisson ratio $\upsilon^S = 0.35$ and solid density $\rho^S = 1200$ kg.m^{-3}. Two-dimensional plane stress condition is assumed for the plate model [22]. The fracture toughness $K_{I,C}$ is prescribed as 16345.7 Pa.m$^{1/2}$ to be consistent with the critical stretch value of 0.1 in PD [22] (assuming a horizon size of $3D_p$). Unlike Rahimi's work [22] where different particle resolutions are used in the fluid and solid bodies, a constant particle size is used in the current work. Two cases are considered here. First, the flexible plate is assumed to be initially flawless, and its dynamic response subjected to fluid pressure from the top is simulated to check the validity of the current FSI model. Next, a vertical crack line is introduced at the middle of the plate, and its rupture behaviour is examined.

Fig. 22 shows the contour plots of the fluid pressure and maximum principal stresses developed in the flexible plate body at different time frames. For the FSI case involving a solid plate with no initial crack, the centre of the plate is deformed downward vertically due to the fluid pressure acting from the top and it rebounds at $t \sim 40$ ms to relax its strain energy. On the other hand, for the plate with a vertical crack line in the middle, it is unable to withstand the fluid pressure and complete failure takes place subsequently at $t \sim 27$ ms. Fig. 23 shows the close-up views on the fractured solid region near the initial crack line. As seen, the region with the highest maximum principal stress is concentrated near the crack tip, and it propagates as the crack grows in the direction perpendicular to the plate axis. Note that there is an apparent gap between the plate body and the neighbouring fluid particles which is due to the numerical artifact of dynamic boundary condition (DBC) adopted in the current work.

The deflections at the middle lower point of the flexible plate predicted using different methods are compared in Fig. 24 (a). The dynamic response of the plate (without the initial crack line) predicted using the current SPH-LPM method compares quite well with that of the SPH-PD method [22]. For the plate with an initial vertical crack at the bottom, complete fracture can be predicted as the deflection speed of the plate undergoes an abrupt change. As observed from Fig. 23 and Fig. 24 (a), complete fracture occurs at $t \sim 27$
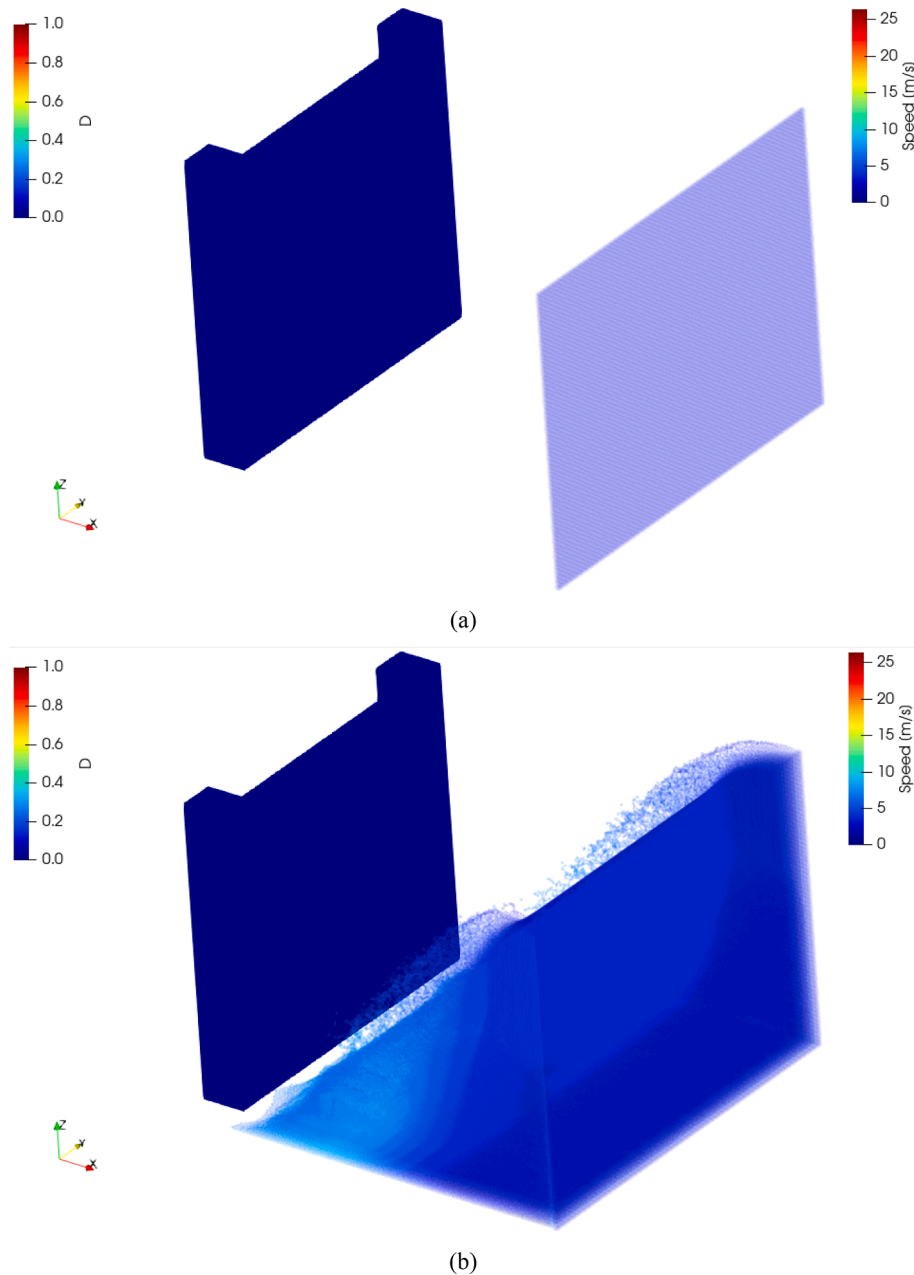
(a)

(b)

Fig. 26. Damage (D) field of the concrete wall of 6 cm thickness subjected to tsunami force at time (a) $t = 0$ s; (b) $t = 0.60$ s; (c) $t = 0.64$ s; (d) $t = 0.65$ s; (e) $t = 0.68$ s and (f) $t = 0.74$ s. The speed of water particles is shown.

ms as deduced from the current SPH-LPM simulation, which is slightly earlier than that predicted using the SPH-PD method [22] of $t \sim 30$ ms. Nevertheless, the agreement between the deflection speeds immediately after the complete rupture predicted using both methods are quite encouraging. The discrepancy in the time instant when complete rupture takes place could be due to the differences in failure criterion and the particle resolution settings in both solvers. As mentioned, for SPH-PD [22], the solid particle spacing is 0.125 mm, and the fluid particle is 8 times larger than the solid particle ($D_p = 1$ mm). As compared to the current SPH-LPM method, a uniform particle spacing is used for both solid and fluid bodies. The sensitivity study of particle sizes: $D_p = 0.0625$ mm, 0.125 mm and 0.25 mm on the deflection at the middle lower point of the plate is performed using the current SPH-LPM method, and it is found that the deflection results show marginal dependence on particle size as shown in Fig. 24 (a).

The sensitivity of using different viscous model is then studied and the result is presented in Fig. 24 (b). It is found that the deflection results simulated using the artificial viscous model (for both $\alpha = 0.01$ and $\alpha = 0.05$) and the real viscous model are almost
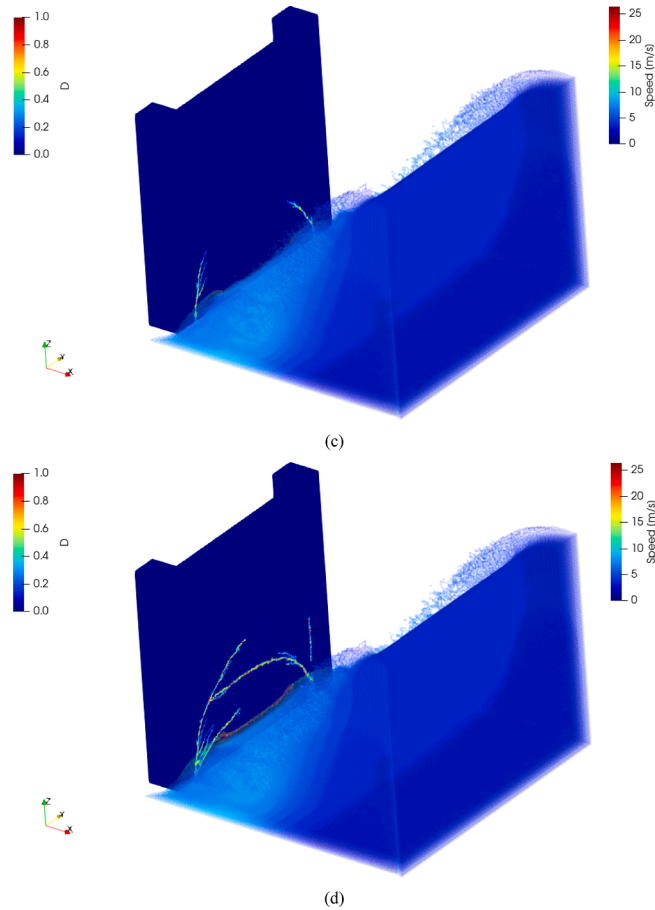
(c)

(d)

Fig. 26. (*continued*).

indiscernible. Therefore, it can be concluded that viscosity does not play a key role in this case, and it could be sufficient to simulate this case using the artificial viscosity approach.

4. Conclusion

Based on the results above, some key conclusions can be summarized as follows:

- By using the Lattice Particle Method (LPM) for brittle solid modelling, the so-called Remove Particle (RP) and Remove Bond (RB) approaches have been used to model the initial crack line. In the current work, a simple mode-I Stress Intensity Factor (SIF) formulation has been proposed for the latter approach and it is found that its accuracy in predicting the static SIF is superior to that of RP.
- For dynamic loading cases, the present SIF model can capture the time evolution of dynamic SIF well, and the results show less numerical oscillations as compared to the previous FEM results.
- Contrary to the maximum principal stress, the mode-I SIF shows insignificant dependence on the particle size as the particle resolution is made finer. This is attractive from the viewpoint of designing a convergent failure model of specimen with cracks.
- The crack path and the crack propagation speed of the dynamic crack branching problem are well captured using the current method. The simulated crack path agrees considerably well with the experimental observation. Nevertheless, the accuracy of the computed mode-I SIF at the crack front particles upon crack branching might be reduced as the crack front particles might not lie at the angular position of $\theta = 45^o$ from the crack line.
- Upon combining the LPM with the Smoothed Particle Hydrodynamics (SPH) technique for fluid flow modelling, several FSI cases involving solid fracture have been successfully simulated, and results are comparable to those simulated using other particle methods. The current SPH-LPM methodology has been implemented in an open-source SPH code, i.e., DualSPHysics which has been optimized in terms of both CPU and GPU performance.

The current SPH-LPM method has been witnessed its potential in simulating FSI problems involving brittle fracture. However, the
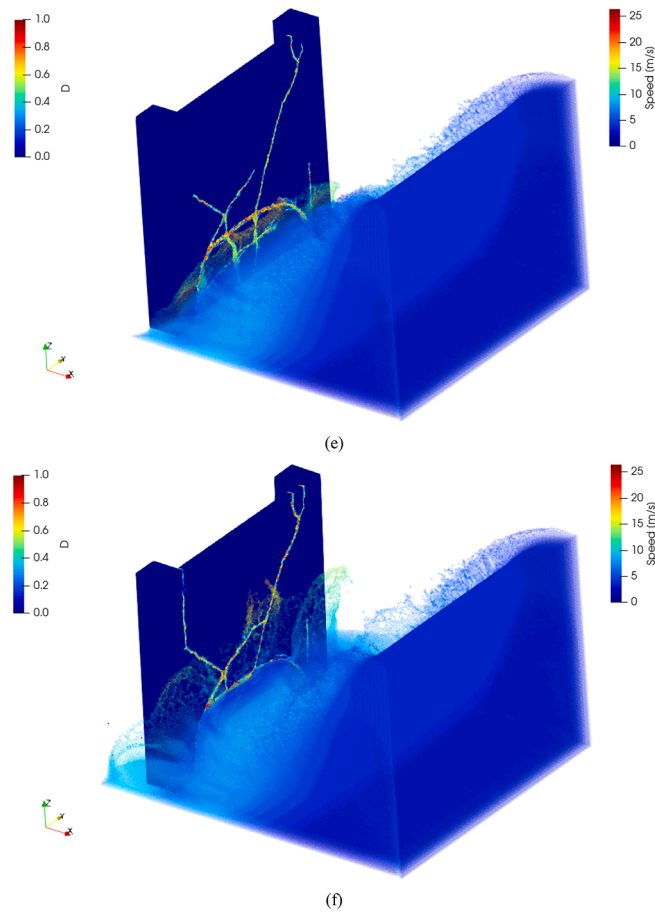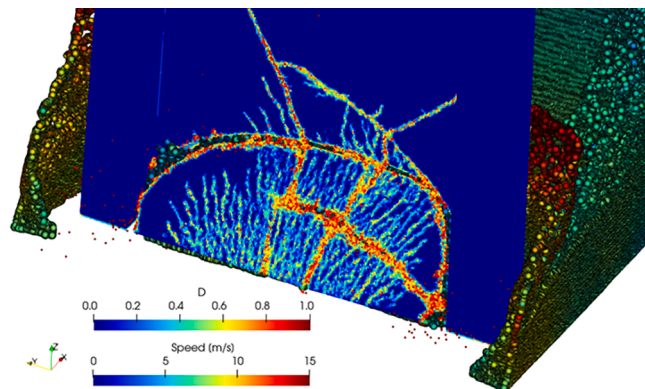
(e)

(f)

Fig. 26. (*continued*).

Fig. 27. Fracturing of concrete wall of thickness 6 cm at $t = 0.74$ s due to tsunami. The speed of water particles is shown.

failure model implemented in the current work is only limited to pure Mode-I fracture mode in 2D, which could limit its capability in simulating real problems involving mixed mode fracture. Other methods such as those based on fracture energy could be implemented. Also, a more robust collision model could be implemented to get rid of the tuning parameter in the current pin-ball collision model. Furthermore, other damage models that account for inelastic deformation such as plasticity could be implemented for studying fracture of ductile materials.

In the Appendix, some of our preliminary simulation results on the level of damage of a 3D concrete structure subjected to a tsunami wave are shown. Our preliminary finding shows that the Rankine failure criterion alone could predict the crack pattern well. This is consistent with the previous finding reported in [39].
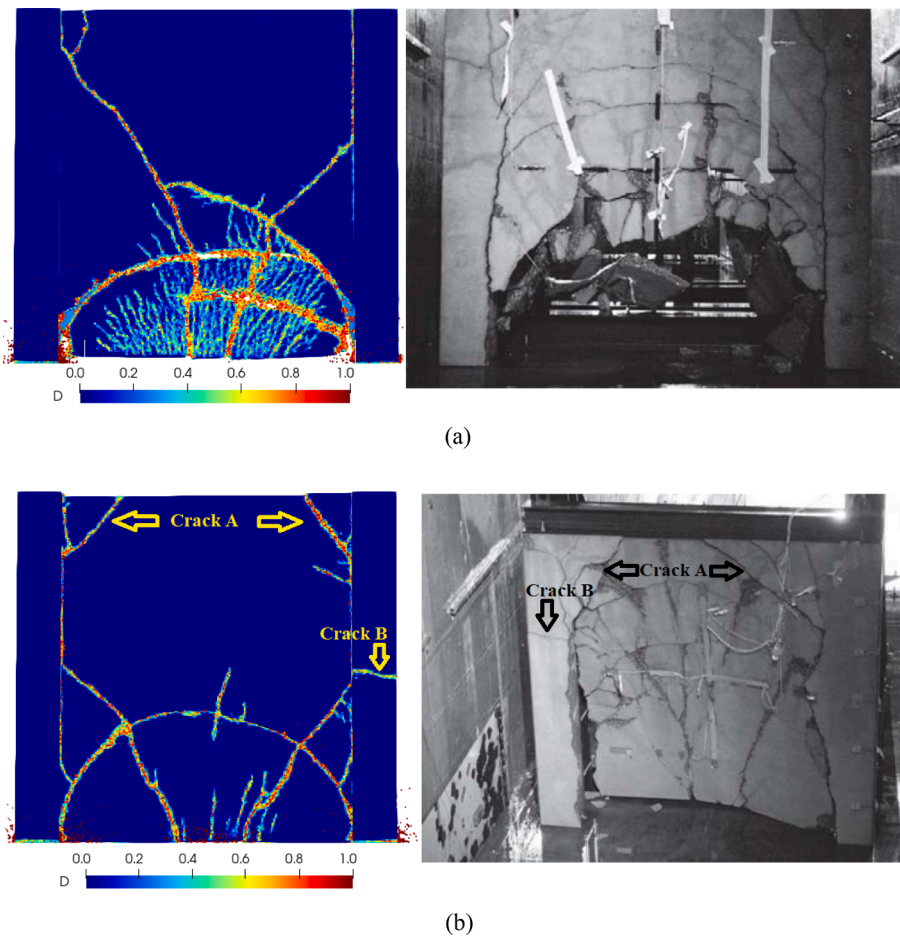
(a)

(b)

Fig. 28. Fractured concrete wall of thickness (a) 6 cm and (b) 10 cm at t = 0.74 s due to tsunami force. Left: 3D SPH-LPM; Right: Experiment [62].

Declaration of Competing Interest

The authors declare the following financial interests/personal relationships which may be considered as potential competing interests: K. C. Ng reports financial support was provided by Malaysia Ministry of Higher Education.

Data availability

Data will be made available on request.

Acknowledgement

Appendix

A1: Collapse of 3D concrete structure due to tsunami force

In this Section, we intend to demonstrate the capability of SPH-LPM in capturing the failure mode of the concrete structure subjected to a strong tsunami force. The failure criterion is purely based on the Rankine criterion, as the fracture mechanics-based model for 3D brittle fracture modelling is still on-going.

This test is inspired by Arikawa [62] where the author had performed a large-scale experiment to generate a tsunami wave with maximum height of ~ 3.5 m via a piston-type wave maker in a long channel of length 184 m for studying the failure mode of a concrete

structure. To reduce the computational cost of the current problem, the full-scale long channel is not modelled. Instead, following Cornejo and co-workers [4], a reduced channel length is considered, and an inlet condition is applied as depicted in Fig. 25. The inlet speed is prescribed as 2.0 ms^{-1}, which is consistent with the maximum speed measured experimentally.

The detailed geometry of the concrete wall is shown in Fig. 25. As shown, both lateral sides of the concrete wall are supported by two concrete columns. The upper and lower sides of the concrete wall, however, are free to move. Note that a thin steel mesh is embedded within the concrete wall in the real experiment [62]. Nevertheless, the steel mesh is not considered in the current work and the concrete structure is modelled as isotropic homogeneous body with material properties [4]: $E = 21$ GPa; $v^S = 0.2$; $\rho^S = 2400$ kg.m^{-3} and $\sigma_{UTS} = 3$ MPa. The particle spacing is set as $D_p = 0.01$ m.

Fig. 26 shows the advancement of the tsunami wave from the water inlet until it hits the concrete structure of thickness 6 cm. It can be observed that once the tsunami wave hits the bottom part of the concrete wall at $t \sim 0.64$ s, two arc-like cracks are formed from the lateral sides of the concrete wall as shown in Fig. 26(c). These two cracks merge subsequently (Fig. 26(d)) and some new cracks are seen to be propagating to the upper part of the concrete wall. Some minor failures are seen at both the lateral supports of the concrete wall as well. Finally, a semi-circular-like hole is formed at the bottom of the concrete wall as the concrete fragments are washed away by the tsunami wave as clearly depicted in Fig. 27 at $t = 0.74$ s. At this time instant, the number of particles is ~ 15 millions.

The crack patterns of the concrete wall of different thicknesses are compared against those observed experimentally in Fig. 28. At wall thickness of 6 cm, a large semi-circular-like hole at the bottom of the concrete wall has been observed experimentally (i.e., so-called punch-shearing failure mode [62]), which agrees well with our current numerical prediction (see Fig. 28(a)). The predicted crack formations at the lateral supports of the concrete wall are tallied with the experimental observation as well. At larger wall thickness of 10 cm, it is anticipated that the concrete wall should be able to sustain more impact force (before it fails), and this would lead to larger bending stress at the lateral supports. As a result, the cracks at the lateral supports of the concrete wall of thickness 10 cm are more apparent as compared to those of thickness 6 cm. Further increase of bending stress would lead to new cracks being formed in the concrete column (see Crack B in Fig. 28(b) for both the numerical and experimental observations), which might lead to failure of the entire concrete structure ultimately. The crack patterns on the concrete wall of thickness 10 cm are compared against the experimental observations in Fig. 28(b). As seen, the predicted semi-circular-like crack pattern at the bottom of the wall is not visually apparent in the experimental photo [62]. The experimentally observed oblique crack patterns at the top (Crack A), however, are clearly captured in the current numerical simulation.

References

[1] Lozovskiy A, Olshanskii MA, Vassilevski YV. Analysis and assessment of a monolithic FSI finite element method. Comput Fluids Jan. 2019;179:277–88. https://doi.org/10.1016/J.COMPFLUID.2018.11.004.

[2] J. Cheng, F. Yu, and L. T. Zhang, 'OpenIFEM: A high performance modular open-source software of the immersed finite element method for fluid-structure interactions', *CMES - Computer Modeling in Engineering and Sciences*, vol. 119, no. 1, pp. 91–124, 2019, 10.32604/cmes.2019.04318.

[3] Greenshields CJ, Weller HG. A unified formulation for continuum mechanics applied to fluid-structure interaction in flexible tubes. Int J Numer Meth Eng 2005; 64(12):1575–93. https://doi.org/10.1002/nme.1409.

[4] Cornejo A, Franci A, Zárate F, Oñate E. A fully Lagrangian formulation for fluid-structure interaction problems with free-surface flows and fracturing solids. Comput Struct 2021;250:106532. https://doi.org/10.1016/j.compstruc.2021.106532.

[5] Elsworth CW. Verification of an overset-grid enabled fluid-structure interaction solver. The Pennsylvania State University; 2014. Master thesis.

[6] Peskin CS. Numerical analysis of blood flow in the heart. J Comput Phys Nov. 1977;25(3):220–52. https://doi.org/10.1016/0021-9991(77)90100-0.

[7] Mittal R, Iaccarino G. Immersed boundary methods. Annu Rev Fluid Mech Jan. 2005;37(1):239–61. https://doi.org/10.1146/annurev.fluid.37.061903.175743.

[8] Ng KC, Hwang YH, Sheu TWH, Yu CH. Moving Particle Level-Set (MPLS) method for incompressible multiphase flow computation. Comput Phys Commun 2015; 196:317–34. https://doi.org/10.1016/j.cpc.2015.06.021.

[9] Lucy LB. A numerical approach to the testing of the fission hypothesis. Astron J 1977;82:1013–24. https://doi.org/10.1007/s13398-014-0173-7.2.

[10] Gingold RA, Monaghan JJ. Smoothed particle hydrodynamics: theory and application to non-spherical stars. MNRAS 1977;181(3):375–89. https://doi.org/10.1093/mnras/181.3.375.

[11] Monaghan JJ. Simulating free surface flows with SPH. J Comput Phys 1994;110(2):399–406. https://doi.org/10.1006/jcph.1994.1034.

[12] Antoci C, Gallati M, Sibilla S. Numerical simulation of fluid-structure interaction by SPH. Comput Struct 2007;85(11–14):879–90. https://doi.org/10.1016/j.compstruc.2007.01.002.

[13] Khayyer A, Shimizu Y, Gotoh H, Nagashima K. A coupled incompressible SPH-Hamiltonian SPH solver for hydroelastic FSI corresponding to composite structures. App Math Model 2021;94:242–74. https://doi.org/10.1016/j.apm.2021.01.011.

[14] Dong X, Huang X, Liu J. 'Modeling and simulation of droplet impact on elastic beams based on SPH'. Eur J Mech A/Solids 2019;75:237–57.

[15] Fourey G, Hermange C, Le Touzé D, Oger G. An efficient FSI coupling strategy between Smoothed Particle Hydrodynamics and Finite Element methods. Comput Phys Commun 2017;217:66–81. https://doi.org/10.1016/j.cpc.2017.04.005.

[16] Li Z, Leduc J, Nunez-Ramirez J, Combescure A, Marongiu JC. A non-intrusive partitioned approach to couple smoothed particle hydrodynamics and finite element methods for transient fluid-structure interaction problems with large interface motion. Comput Mech 2015;55(4):697–718. https://doi.org/10.1007/s00466-015-1131-8.

[17] Yang Q, Jones V, McCue L. Free-surface flow interactions with deformable structures using an SPH-FEM model. Ocean Engng 2012;55:136–47. https://doi.org/10.1016/j.oceaneng.2012.06.031.

[18] O'Connor J, Rogers BD. A fluid–structure interaction model for free-surface flows and flexible structures using smoothed particle hydrodynamics on a GPU. J Fluids Struct 2021;104:103312. https://doi.org/10.1016/j.jfluidstructs.2021.103312.

[19] Zhan L, Peng C, Zhang B, Wu W. A stabilized TL–WC SPH approach with GPU acceleration for three-dimensional fluid–structure interaction. J Fluids Struct 2019;86:329–53. https://doi.org/10.1016/j.jfluidstructs.2019.02.002.

[20] Han L, Hu X. SPH modeling of fluid-structure interaction. J Hydrodyn 2018;30(1):62–9. https://doi.org/10.1007/s42241-018-0006-9.

[21] Dong X, Liu Y, Yu R, Fan M. Simulation of droplet bouncing on flexible substrate in 2D and 3D with WC-TL SPH method. J Fluids Struct 2023;119:103864.

[22] Rahimi MN, Kolukisa DC, Yildiz M, Ozbulut M, Kefal A. A generalized hybrid smoothed particle hydrodynamics–peridynamics algorithm with a novel Lagrangian mapping for solution and failure analysis of fluid–structure interaction problems. Comput Methods Appl Mech Eng 2022;389:114370. https://doi.org/10.1016/j.cma.2021.114370.

[23] Wu K, Yang D, Wright N. A coupled SPH-DEM model for fluid-structure interaction problems with free-surface flow and structural failure. Comput Struct 2016; 177:141–61. https://doi.org/10.1016/j.compstruc.2016.08.012.

[24] Wu K, Yang D, Wright N, Khan A. An integrated particle model for fluid–particle–structure interaction problems with free-surface flow and structural failure. J Fluids Struct 2018;76:166–84. https://doi.org/10.1016/j.jfluidstructs.2017.09.011.

[25] Wu Z, Yu F, Zhang P, Liu X. Micro-mechanism study on rock breaking behavior under water jet impact using coupled SPH-FEM/DEM method with Voronoi grains. Engng Anal Bound Elem 2019;108:472–83. https://doi.org/10.1016/j.enganabound.2019.08.026.

[26] Yao X, Huang D. Coupled PD-SPH modeling for fluid-structure interaction problems with large deformation and fracturing. Comput Struct 2022;270:106847. https://doi.org/10.1016/j.compstruc.2022.106847.

[27] Ng KC, Alexiadis A, Chen H, Sheu TWH. A coupled Smoothed Particle Hydrodynamics-Volume Compensated Particle Method (SPH-VCPM) for Fluid Structure Interaction (FSI) modelling. Ocean Engng 2020;218:107923.

[28] Chen H, Lin E, Liu Y. A novel Volume-Compensated Particle method for 2D elasticity and plasticity analysis. Int J Solids Struct May 2014;51(9):1819–33. https://doi.org/10.1016/j.ijsolstr.2014.01.025.

[29] Chen H, Lin E, Jiao Y, Liu Y. A generalized 2D non-local lattice spring model for fracture simulation. Comput Mech 2014;54(6):1541–58. https://doi.org/10.1007/s00466-014-1075-4.

[30] Tavarez FA, Plesha ME. Discrete element method for modelling solid and particulate materials. Int J Numer Meth Engng Apr. 2007;70(4):379–404. https://doi.org/10.1002/nme.1881.

[31] Ganesh KV, Islam MRI, Patra PK, Travis KP. A pseudo-spring based SPH framework for studying fatigue crack propagation. Int J Fatigue Sep. 2022;162:106986. https://doi.org/10.1016/J.IJFATIGUE.2022.106986.

[32] Tazoe K, Tanaka H, Oka M, Yagawa G. Analyses of fatigue crack propagation with smoothed particle hydrodynamics method. Engng Fract Mech 2020;228: 106819.

[33] K. Tazoe, H. Tanaka, M. Oka, and G. Yagawa, 'An analysis of half elliptical surface crack propagation phenomenon with smoothed particle hydrodynamics method', in *International Conference on Particle-based Methods – Fundamentals and Applications*, 2017, pp. 890–897.

[34] Ng KC, Low WC, Chen H, Tafuni A, Nakayama A. A three-dimensional fluid-structure interaction model based on SPH and lattice-spring method for simulating complex hydroelastic problems. Ocean Engng 2022;260:112026. https://doi.org/10.1016/j.oceaneng.2022.112026.

[35] Chen H, Liu Y. A non-local 3D lattice particle framework for elastic solids. Int J Solids Struct Mar. 2016;81:411–20. https://doi.org/10.1016/j.ijsolstr.2015.12.026.

[36] Low WC, Ng KC, Ng HK. A SPH-lattice spring method for modelling Fluid Structure Interaction involving composite body and free surface. Comput Part Mech 2023. https://doi.org/10.1007/s40571-023-00576-z.

[37] Grah M, Alzebdeh K, Sheng PY, Vaudin MD, Bowman KJ, Ostoja-Starzewski M. Brittle intergranular failure in 2D microstructures: Experiments and computer simulations. Acta Mater 1996;44(10):4003–18. https://doi.org/10.1016/S1359-6454(96)00044-4.

[38] Schlangen E, Garboczi EJ. New method for simulating fracture using an elastically uniform random geometry lattice. Int J Engng Sci 1996;34(10):1131–44. https://doi.org/10.1016/0020-7225(96)00019-5.

[39] Yao W-W, Zhou X-P, Berto F. Continuous smoothed particle hydrodynamics for cracked nonconvex bodies by diffraction criterion. Theor Appl Fract Mech 2020; 108:102584.

[40] Wiragunarsa IM, Zuhal LR, Dirgantara T, Putra IS. A particle interaction-based crack model using an improved smoothed particle hydrodynamics for fatigue crack growth simulations. Int J Fract 2021;229(2):pp. https://doi.org/10.1007/s10704-021-00553-8.

[41] C. T. Sun and Z. H. Jin, *Fracture Mechanics*. Elsevier, 2012. 10.1016/C2009-0-63512-1.

[42] Wang F, Wang M, Nezhad MM, Qiu H, Ying P, Niu C. Rock dynamic crack propagation under different loading rates using improved single cleavage semi-circle specimen. Appl Sci (Switzerland) 2019;9(22):pp. https://doi.org/10.3390/APP9224944.

[43] Antuono M, Colagrossi A, Marrone S, Molteni D. Free-surface flows solved by means of SPH schemes with numerical diffusive terms. Comput Phys Commun 2010;181(3):532–49.

[44] Wendland H. Piecewise polynomial, positive definite and compactly supported radial functions of minimal degree. Adv Computat Math 1995;4(1):389–96.

[45] Antuono M, Colagrossi A, Marrone S. Numerical diffusive terms in weakly-compressible SPH schemes. Comput Phys Commun 2012;183(12):2570–80. https://doi.org/10.1016/j.cpc.2012.07.006.

[46] Fourtakas G, Dominguez JM, Vacondio R, Rogers BD. Local uniform stencil (LUST) boundary condition for arbitrary 3-D boundaries in parallel smoothed particle hydrodynamics (SPH) models. Comput Fluids 2019;190:346–61. https://doi.org/10.1016/j.compfluid.2019.06.009.

[47] Batchelor GK. In: An Introduction to Fluid Dynamics. Cambridge University Press; 2000. https://doi.org/10.1017/CBO9780511800955.

[48] Dalrymple RA, Rogers BD. Numerical modeling of water waves with the SPH method. Coast Engng 2006;53(2–3):141–7.

[49] Crespo AJC, Domínguez JM, Rogers BD, Gómez-Gesteira M, Longshaw S, Canelas R, et al. DualSPHysics: Open-source parallel CFD solver based on Smoothed Particle Hydrodynamics (SPH). Comput Phys Commun 2015;187:204–16.

[50] Crespo AJC, G'mez-Gesteira M, Dalrymple RA. Boundary conditions generated by dynamic particles in SPH methods. Computers, Materials and Continua 2007. https://doi.org/10.3970/cmc.2007.005.173.

[51] Ng KC, Alexiadis A, Ng YL. An improved particle method for simulating Fluid-Structure Interactions: The multi-resolution SPH-VCPM approach. Ocean Engng 2022;247(January):110779. https://doi.org/10.1016/j.oceaneng.2022.110779.

[52] Gunawan FE, Homma H, Adhikari B. Nugget Strength of Spot Weld under Shear Impact Load. J Solid Mech Mater Eng 2008;2(8):1136–45. https://doi.org/10.1299/jmmp.2.1136.

[53] Menouillard T, Song JH, Duan Q, Belytschko T. Time dependent crack tip enrichment for dynamic crack propagation. Int J Fract Mar. 2010;162(1–2):33–49. https://doi.org/10.1007/s10704-009-9405-9.

[54] Liu ZL, Menouillard T, Belytschko T. An XFEM/Spectral element method for dynamic crack propagation. Int J Fract Jun. 2011;169(2):183–98. https://doi.org/10.1007/s10704-011-9593-y.

[55] Song JH, Wang H, Belytschko T. A comparative study on finite element methods for dynamic fracture. Comput Mech 2008;42(2):239–50. https://doi.org/10.1007/s00466-007-0210-x.

[56] Ramulu M, Kobayashi AS. Mechanics of crack curving and branching - a dynamic fracture analysis. Int J Fract Mar. 1985;27(3–4):187–201. https://doi.org/10.1007/BF00017967.

[57] Song JH, Belytschko T. Cracking node method for dynamic fracture with finite elements. Int J Numer Meth Engng Jan. 2009;77(3):360–85. https://doi.org/10.1002/nme.2415.

[58] Bowden FP, Brunton JH, Field JE, Heyes AD. Controlled fracture of brittle solids and interruption of electrical current. Nature 1967;216(5110):pp. https://doi.org/10.1038/216038a0.

[59] Belytschko T, Yeh IS. The splitting pinball method for contact-impact problems. Comput Methods Appl Mech Engng 1993;105(3):375–93. https://doi.org/10.1016/0045-7825(93)90064-5.

[60] Rushdie M, Islam I, Peng C. A Total Lagrangian SPH Method for Modelling Damage and Failure in Solids. Int J Mech Sci 2019;157–158:498–511.

[61] A.F. Bower, *Applied mechanics of solids*. 2009. 10.1201/9781439802489.

[62] Arikawa T. Structural Behavior under Impulsive Tsunami Loading. J Disaster Res 2009;4(6):377–81.